JOURNAL OF GUIDANCE, CONTROL, AND DYNAMICS
Vol. 34, No. 1, January–February 2011

# Length Scaling in Spacecraft Dynamics

Justin A. Atchison* and Mason A. Peck†
*Cornell University, Ithaca, New York 14853*

DOI: 10.2514/1.49383

**Length-scaling represents a new degree of freedom for spacecraft mission design. This paper presents a method for comparing the length scales of arbitrary spacecraft and uses this approach to evaluate the relevance of 12 environmental forces and torques. Three sample spacecraft geometries are considered: a sphere, a cube, and a thin square plate, at three near-Earth altitudes: 500, 1000, and 10,000 km. This analysis offers a guide for orbit and attitude simulations of small bodies, by suggesting which effects can and cannot be neglected for a given environment and error tolerance. This approach to length scaling may enable extremely small spacecraft to exploit unfamiliar dynamic behaviors that result in solar sail maneuvers, atmospheric reentry, and Lorentz propulsion.**

## Nomenclature

$A_C$ = cross-sectional area
$A_S$ = surface area
$\boldsymbol{a}$ = translational acceleration
$\boldsymbol{\alpha}$ = angular acceleration
$\boldsymbol{B}$ = magnetic field
$\boldsymbol{b}_i$ = one of a set of body-fixed orthogonal axes
$C$ = self-capacitance
$c$ = speed of light in a vacuum
$c_p$ = specific heat
$d$ = thickness
$\boldsymbol{F}$ = force acting on a body
$G_p$ = gravitational defocusing factor
$I$ = mass moment of inertia for a body's mass center
$i$ = electrical current
$Kn$ = Knudsen number
$\hat{\boldsymbol{L}}$ = direction of aerodynamic lift
$l_M$ = conductor length
$\boldsymbol{M}$ = magnetic dipole moment
$m$ = mass
$\boldsymbol{n}$ = surface-normal vector
$n_M$ = number of coils in an electromagnet
$\boldsymbol{P}$ = pressure
$P_s$ = pressure associated with solar flux
$Q$ = thermal energy
$q$ = electrostatic charge
$Re$ = Reynolds number
$R_p$ = planetary radius
$\boldsymbol{r}$ = position vector from the gravitational barycenter to the spacecraft mass center
$T$ = temperature
$\boldsymbol{\tau}$ = torque acting on a body
$t$ = time
$\boldsymbol{v}$ = orbital velocity, time derivative of $\boldsymbol{r}$
$v_w$ = surface-normal velocity of molecule
$W_0$ = solar energy flux at distance $r_0$ from the sun
$\chi$ = electrical resistance
$\beta_{\mathrm{SP}}$ = solar pressure lightness number
$\beta_{\mathrm{AD}}$ = ballistic coefficient
$\Gamma$ = universal gas constant
$\gamma$ = single-axis attitude (angle of a body-fixed vector relative to a single reference)
$\boldsymbol{\delta}_{\mathrm{cm}}$ = position vector of an expected mass center measured relative to a body's actual mass center
$\boldsymbol{\delta}_{\mathrm{cp}}$ = position vector of a center of pressure relative to a body's mass center
$\boldsymbol{\delta}_F$ = position vector to the point of a force's application, measured relative to a body's mass center
$\varepsilon_0$ = permittivity of free space
$\zeta$ = mean free path
$\eta$ = optical coefficient for simpler reflection/absorption model
$\eta_{\mathrm{ab}}$ = optical coefficient associated with absorption
$\eta_{\mathrm{dr}}$ = optical coefficient associated with diffuse reflection
$\eta_{n,t}$ = normal and tangential momentum-accommodation coefficients
$\eta_p$ = planetary Bond albedo
$\eta_{\mathrm{sr}}$ = optical coefficient associated with specular reflection
$\kappa$ = dimensionless scale factor associated with geometry
$\lambda$ = characteristic length of a body
$\mu$ = a central body's gravitational constant
$\xi$ = material nondirectional emissivity
$\rho$ = mass density
$\rho_A$ = atmosphere density
$\sigma$ = material resistivity
$\varphi$ = electric potential
$\Omega$ = magnetization
$\boldsymbol{\omega}$ = angular velocity vector

*Subscripts*

AD = aerodynamic drag
AL = aerodynamic lift
EC = eddy current
$G$ = gravity
LZ = Lorentz Force
$M$ = magnetic attraction or repulsion
PA = planetary albedo
PC = particle collisions
PR = Poynting–Robertson drag
$p$ = planetary
SP = solar radiation pressure
SW = solar wind
TE = thermal emission

## I. Introduction

SPACECRAFT length scale determines the magnitude of many accelerations for which the space environment is responsible. For spacecraft designers and mission engineers, this scaling drives common mission concerns, such as orienting a spacecraft to minimize aerodynamic drag effects or determining the magnitude of

Received 15 February 2010; revision received 30 August 2010; accepted for publication 20 September 2010. 

*Graduate Research Assistant, Sibley School of Mechanical and Aerospace Engineering, 245 Upson Hall. Student Member AIAA.

†Assistant Professor, Sibley School of Mechanical and Aerospace Engineering, 212 Upson Hall. Member AIAA.

disturbance accelerations. Instead of neglecting these effects or merely accommodating them, this research seeks to exploit length scaling to achieve novel mission opportunities. The following analysis surveys most near-Earth environmental accelerations and describes a spacecraft architecture whose length scale maximizes their benefits.

This work is inspired by research in interplanetary dust dynamics as well as advances in microfabrication techniques. Continually shrinking electronics and sensors have created a "smaller is better" paradigm. Naturally, smaller size tends to reduce weight and power, which benefits any aerospace system. While such advances enable the fabrication of an extremely small spacecraft, results from the interplanetary dust community justify such activity. Dust particles, by virtue of a characteristic size on the order of tens of microns, experience highly non-Keplerian orbit dynamics. Solar-radiation pressure has been found to eject dust from the solar system [1–3], electromagnetic effects capture and eject dust in planet-centered orbits [4,5], and aerodynamic drag captures and lands dust without the bright hypersonic ablation characteristic of larger meteors [6,7]. Such effects are passive. This research is aimed at exploiting such small-body effects actively in new operations concepts.

There are other compelling reasons to develop extremely small spacecraft: economies of production, reduced launch mass, and distributed sensing opportunities. Some research has focused on developing technologies to enable a monolithic integrated-circuit (IC) silicon spacecraft design [8–15]. This architecture, sometimes called a "spacecraft-on-a-chip," capitalizes on advances in IC and microelectrochemical systems technologies. Barnhart et al. [8] provides an historical summary of these efforts.

The present work seeks to qualify and quantify the dependence of length scale on the orbital and angular accelerations experienced by a spacecraft in Earth orbit. A framework of scaling is introduced that generalizes an arbitrary spacecraft geometry to a series of nondimensional coefficients. Using this framework, 12 environmental perturbations are modeled for the near-Earth space environment. This modeling follows Longuski et al.'s survey of nongravitational accelerations on the Galileo spacecraft, which focuses on order-of-magnitude calculations [16]. The sources of these perturbations are associated with gravity, particle collisions, radiation, and magnetic fields. The environmental accelerations are considered for three simple and applicable geometries: a sphere, a cube, and a thin square plate. Using these test cases, the analysis relates the relative importance of each acceleration on spacecraft orbital and angular dynamics, across a range of length scales. These results suggest sample mission applications for an IC spacecraft-on-a-chip, including solar sailing, atmospheric reentry, and Lorentz propulsion.

## II. Geometric and Kinematic Scaling

The geometry of a body of interest can be decoupled into functions of length scale and dimensionless parameters. Here, units of length are generalized into a single variable $\lambda$, the characteristic length of the spacecraft. For example, the volume $V$ of a sample spacecraft is taken as the characteristic volume $\lambda^3$ scaled by a dimensionless factor $\kappa_V$:

$$V = \kappa_V \lambda^3 \tag{1}$$

The spacecraft's mass $m$ is the product of its volume and mean mass density $\rho$:

$$m = \kappa_V \rho \lambda^3 \tag{2}$$

The density and scale factor are taken to be constant properties of the spacecraft, while $\lambda$ is an independent variable. The cross-sectional area and total surface area can be defined using $\kappa_C$ and $\kappa_S$, respectively:

$$A_C = \kappa_C \lambda^2 \tag{3}$$

**Table 1 Dimensionless scale factors**

| Scale factor | Sphere | Cube | Thin square plate |
|---|---|---|---|
| $\kappa_V$ | $\frac{\pi}{6}$ | 1 | $\kappa_\varepsilon$ |
| $\kappa_I$ | $\frac{\pi}{60}$ | $\frac{1}{6}$ | $\frac{\kappa_\varepsilon}{12}, \frac{\kappa_\varepsilon}{6}$ |
| $\kappa_C$ | $\frac{\pi}{4}$ | 1 | 1 |
| $\kappa_S$ | $\pi$ | 6 | 2 |

$$A_S = \kappa_S \lambda^2 \tag{4}$$

Likewise, a mass moment of inertia $I$ about the spacecraft's mass center can be treated as the product of the density and $\lambda^5$, scaled by an appropriate coefficient $\kappa_I$:

$$I = \kappa_I \rho \lambda^5 \tag{5}$$

Table 1 gives the dimensionless scale factors $\kappa_i$ for three geometries of interest: a sphere, a cube, and a thin square plate. Figure 1 shows these shapes with body-fixed basis vectors $\boldsymbol{b}_i$. For a sphere, a shape that resembles many dust particles [2], the characteristic length is taken to be the diameter. For a cube-shaped body (e.g. the aptly named CubeSat [17]) $\lambda$ is taken to be the side length. Finally, for a thin square plate that evokes spacecraft-on-chip architectures, $\lambda$ is the length of a side. While the descriptions of the sphere and cube are one-dimensional, two parameters fully describe the square plate: the side length and the thickness. These two parameters are related by the constant aspect ratio $\kappa_\varepsilon$, the ratio of the thickness of the plate $d$ to the side length $\lambda$ of the square:

$$\kappa_\varepsilon \equiv \frac{d}{\lambda}, \qquad \kappa_\varepsilon \ll 1$$

Previous studies [10,11] have suggested an IC spacecraft-on-chip architecture with a side length of 1 cm and a thickness of 25 $\mu$m. This combined length and thickness yields a value of $\kappa_\varepsilon = 0.0025$.

A ratio that appears in many environmental accelerations is the cross-sectional area-to-mass ratio:

$$\frac{A_C}{m} = \frac{\kappa_C}{\kappa_V \rho} \lambda^{-1} \tag{6}$$

The ratio depends on length scale indirectly and geometry via $\kappa_C/\kappa_V$. For a sphere and cube, $\kappa_C/\kappa_V$ reduces to a constant value of 1.5 and 1.0, respectively. For a thin square plate, $\kappa_C/(\kappa_V \lambda)$ reduces to the plate's thickness $d = \kappa_\epsilon \lambda$.

The sphere and the cube have triaxial symmetry; mass moments of inertia of such a body are equal for any axis passing through the mass center. The inertia matrix $\boldsymbol{I}$ for a triaxially symmetric body can be expressed as a scalar multiple of the identity matrix:

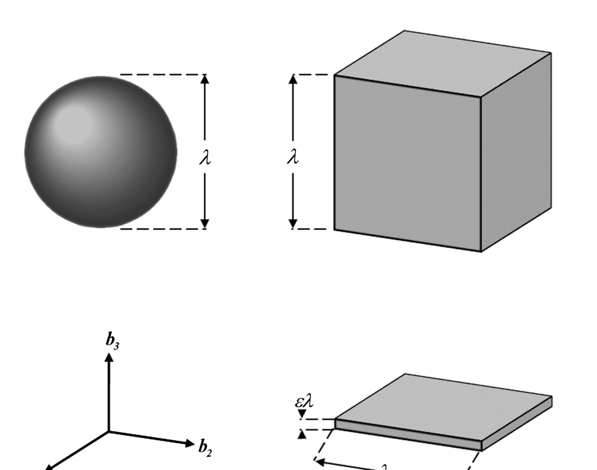


**Fig. 1 Characteristic length and axis of rotation for geometries of interest: sphere, cube, and thin square plate.**

$$\boldsymbol{I} = \kappa_I \rho \lambda^5 1_{3\times3} \tag{7}$$

The thin square plate has biaxial symmetry. In $\boldsymbol{b}_i$ axes, which are chosen to align with the principal axes of the plate, the inertia about the mass center is

$$\boldsymbol{I}_{\text{plate}} = \kappa_I \rho \lambda^5 \text{diag}(1,1,2) \tag{8}$$

Scaling also appears in the orbital and attitude equations of motion. Newton's second law, written in terms of acceleration, includes an implicit dependence on $\lambda$:

$$a = \frac{F}{m} = \frac{F}{\kappa_V \rho} \lambda^{-3} \tag{9}$$

Likewise $\lambda$ appears in angular accelerations. Angular acceleration is related to torque $\boldsymbol{\tau}$ according to Euler's equation of motion for a rigid body [18]:

$$\boldsymbol{I} \cdot \dot{\boldsymbol{\omega}} + \boldsymbol{\omega} \times \boldsymbol{I} \cdot \boldsymbol{\omega} = \boldsymbol{\tau} \tag{10}$$

For triaxially symmetric geometries, as in the sphere and cube, $\boldsymbol{\omega} \times \boldsymbol{I} \cdot \boldsymbol{\omega}$ reduces to 0. Alternatively, for nonsymmetric geometries, one can consider the case of slow spin, $I\omega^2 \ll \tau$, with nutation damping. These cases simplify the analysis, such that angular acceleration $\alpha \equiv \dot{\omega}$ is proportional to $I$:

$$\alpha = \frac{\tau}{I} \tag{11}$$

$\alpha$ can be thought of as the ratio of torque to inertia, or as the angular acceleration for one-dimensional cases.

Often the torque of interest is caused by a force acting at a point $\boldsymbol{\delta}_F$ measured from the spacecraft's mass center:

$$\boldsymbol{\tau} = \boldsymbol{\delta}_F \times \boldsymbol{F} \tag{12}$$

A scale factor $\kappa_T$ can be defined to account for both the location and orientation of the force's application, yielding a scalar equation in terms of $\lambda$:

$$\tau = \kappa_T F \lambda \tag{13}$$

For most practical cases, $\kappa_T$ changes often. Here, $\kappa_T$ is treated as a parameter whose value is fixed for a given case. This choice enables different torques to be compared in terms of their dependence on $\lambda$. With this framework of dimensionless constants, a spacecraft's sensitivity to characteristic length can be explored in terms of each environmental force and torque model.

## III. Gravity

The following analysis verifies that gravitational accelerations are uniquely length-independent and suggests that the opportunities and challenges associated with gravity gradient torques, $n$-body maneuvers, and planetary oblateness effects are present at any length scale.

### A. Two-Body Orbits

Newton's Law of Universal Gravitation gives the force acting between two bodies:

$$\boldsymbol{F}_G = -\frac{\mu}{r^2} m \hat{\boldsymbol{r}} \tag{14}$$

where the substitution $\mu = Gm_p$ is the product of the universal gravitational constant $G$ and the opposing body's mass $m_p$. The magnitude of this force scales with the spacecraft's mass and thus with $\lambda^3$:

$$F_G = \kappa_V \rho \frac{\mu}{r^2} \lambda^3 \tag{15}$$

The acceleration is the familiar, length-independent right-hand side of the two-body equation of motion:

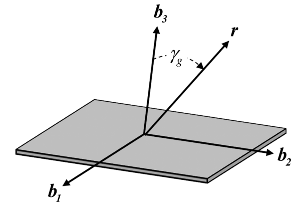


**Fig. 2 Angle of rotation associated with gravity gradient torques.**

$$\boldsymbol{a}_G = -\frac{\mu}{r^2} \hat{\boldsymbol{r}} \tag{16}$$

As long as $m \ll m_p$, the characteristic size of the orbiting body is unimportant.

Gravitational force is said to act at a body's center of gravity, a point that can differ from a body's center of mass because gravity depends on distance from the central body. As a result, the force due to gravity can apply the familiar gravity gradient torque. This torque is related to the body's inertia tensor and the direction of the gravitational acceleration $-\hat{\boldsymbol{r}}$ [19]:

$$\boldsymbol{\tau} = \frac{3\mu}{r^3} (\hat{\boldsymbol{r}} \times \boldsymbol{I} \cdot \hat{\boldsymbol{r}}) \boldsymbol{G} \tag{17}$$

For a sphere or cube, triaxial symmetry reduces the vector product $\hat{\boldsymbol{r}} \times \boldsymbol{I} \cdot \hat{\boldsymbol{r}}$ to 0 for any attitude, indicating that there is no applied torque. For the thin square plate, rotation about any axis perpendicular to $\boldsymbol{b}_3$, as illustrated in Fig. 2, reduces this term to $\|\hat{\boldsymbol{r}} \times \boldsymbol{I} \cdot \hat{\boldsymbol{r}}\| = I_1 \cos\gamma_G \sin\gamma_G$ where $\cos\gamma_G = \hat{\boldsymbol{r}} \cdot \boldsymbol{b}_3$. The zero-torque equilibria are at $\gamma_G = k\frac{\pi}{2}$, where $k$ is an integer. Odd values of $k$ represent marginally stable equilibria; even values of $k$ represent unstable equilibria. More simply, gravity gradient torques tend to orient a square plate such that $\hat{\boldsymbol{r}} \perp \boldsymbol{b}_3$.

A mass imbalance can introduce unexpected gravity gradient torque. For a deviation $\boldsymbol{\delta}_{\text{cm}}$ of the mass from the expected mass center, the parallel-axis theorem gives the inertia $\boldsymbol{I}_\delta$ about the shifted mass center [18]:

$$\boldsymbol{I}_\delta = \boldsymbol{I} + m(\boldsymbol{\delta}_{\text{cm}}^2 1_{3\times3} - \boldsymbol{\delta}_{\text{cm}} \boldsymbol{\delta}_{\text{cm}}) \tag{18}$$

This results in a gravity gradient torque proportional to $(m\hat{\boldsymbol{r}} \times \boldsymbol{\delta}_{\text{cm}} \boldsymbol{\delta}_{\text{cm}} \cdot \hat{\boldsymbol{r}})$, a term that goes to zero as $\boldsymbol{\delta}_{\text{cm}} \| \hat{\boldsymbol{r}}$. For a plate geometry with a mass center displacement in the $\boldsymbol{b}_1$-$\boldsymbol{b}_2$ plane, the magnitude of the resultant torque goes with $\kappa_V \lambda^3 \boldsymbol{\delta}_{\text{cm}}^2 \cos\gamma_G \sin\gamma_G$, with equilibria at $\hat{\boldsymbol{r}} \perp \boldsymbol{b}_3$ and $\boldsymbol{\delta}_{\text{cm}} \| \hat{\boldsymbol{r}}$.

### B. Higher-Order Gravitational Accelerations

Gravity is also responsible for effects such as accelerations associated with secondary bodies [19], central body nonspherical mass distribution [20], general relativity [21], Lense–Thirring frame-dragging [21,22], and ocean and planetary tides [23]. In each of these cases, the accelerations are still length-independent. Any maneuver based on these physics, such as a low-energy transfer orbit, is equally possible for a small or large spacecraft.

## IV. Particle Collisions

Spacecraft accelerate when they collide with very small particles. These particles are associated with atmospheres, interplanetary dust, and solar wind. The accelerations that these collisions produce scale with $A_C/m$, implying that the associated acceleration depends on $\lambda^{-1}$. A smaller body is more sensitive than a large body to particle-collision accelerations.

Given a spacecraft that is much larger than the mean distance between particles, collision forces can be modeled as a pressure that acts at an effective center of pressure $\boldsymbol{\delta}_{\text{CP}}$. For the regular shapes considered here, this force acts through the center of mass. Therefore, these three shapes experience torque-free particle collisions. In practice, an arbitrarily small dislocation of $\boldsymbol{\delta}_{\text{CP}}$ produces a torque of the form in Eq. (12). This torque scales with $\lambda^3$, resulting in an

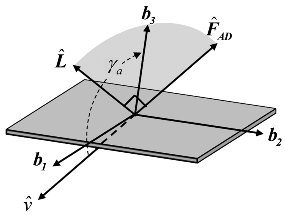


**Fig. 3 Orientation of lift and drag forces on a flat plate in a fluid flow.**

angular acceleration that scales with $\lambda^{-2}$. If the spacecraft is sufficiently small (e.g. at the $\lambda$ of the particles themselves), particle collisions are more rare and no longer accurately modeled as a pressure.

### A. Aerodynamic Forces

Bodies traveling through an atmosphere experience aerodynamic forces. In the rarefied upper atmosphere that spacecraft in low Earth orbits (LEO) experience, aerodynamic drag often dominates the non-gravitational accelerations. This drag acts in the direction opposite velocity, removing energy and angular momentum from the orbit [23]. Here, drag is evaluated in a model with simplified, hyperthermal, free-molecular flow that neglects spinning and tumbling body effects. The force's magnitude is proportional to the body's cross-sectional area, a quantity that scales with $\lambda^2$ [23]:

$$\boldsymbol{F}_{\mathrm{AD}} = -\frac{1}{2}\kappa_{\mathrm{AD}} A_C \rho_A v^2 \hat{\boldsymbol{v}} \tag{19}$$

The local atmospheric density is given by $\rho_a$, a quantity that encapsulates the force's strong dependence on altitude and solar activity. Some shapes also experience aerodynamic lift, which takes a form similar to that of aerodynamic drag [23]:

$$\boldsymbol{F}_{\mathrm{AL}} = -\frac{1}{2}\kappa_{\mathrm{AL}} A_C \rho_A v^2 \hat{\boldsymbol{L}} \tag{20}$$

This force is directed along $\hat{\boldsymbol{L}}$, a vector perpendicular to $\hat{\boldsymbol{v}}$ and in the plane of $\boldsymbol{F}_{\mathrm{AD}}$ and $\boldsymbol{b}_3$, as illustrated in Fig. 3.

The coefficients of drag $\kappa_{\mathrm{AD}}$ and lift $\kappa_{\mathrm{AL}}$ account for the surface interactions associated with diffuse and specular reflection, as well as molecular accommodation, the proportion of momentum imparted by the impacting molecules [24]. Table 2 gives characteristic values these coefficients. A flat plate behaves like an airfoil in that it has coefficients that vary with attitude. Here, the so-called angle of attack is referenced to $\boldsymbol{b}_3$, $\cos\gamma_A = \boldsymbol{b}_3 \cdot \hat{\boldsymbol{v}}$. Storch gives equations for $\kappa_{\mathrm{AD}}$ and $\kappa_{\mathrm{AL}}$ for a flat plate in hyperthermal free-molecular flow. These equations, in terms of $\gamma_A$, are [24]

$$\kappa_{\mathrm{AD}} = 2\left[\eta_t + \eta_n \frac{v_w}{v}\cos(\gamma_A) + (2-\eta_n-\eta_t)\cos^2(\gamma_A)\right]\cos(\gamma_A) \tag{21}$$

$$\kappa_{\mathrm{AL}} = \left[\eta_n \frac{v_w}{v} + (2-\eta_n-\eta_t)\cos(\gamma_A)\right]\sin(2\gamma_A) \tag{22}$$

Molecular accommodation is modeled with the normal and tangential momentum-accommodation coefficients $\eta_n$ and $\eta_t$ respectively. They are a function of both the surface and fluid properties. The normal component of the thermal velocity of molecules escaping the plate's surface $v_w$ is given by [24]

**Table 2 Coefficients of drag and lift for geometries of interest**

| Scale factor | Sphere [25,26] | Cube [25] | Thin square plate [24] |
|---|---|---|---|
| $\kappa_{\mathrm{AD}}$ | 2.2 | 2.2 | Equation (21) |
| $\kappa_{\mathrm{AL}}$ | 0 | 0 | Equation (22) |

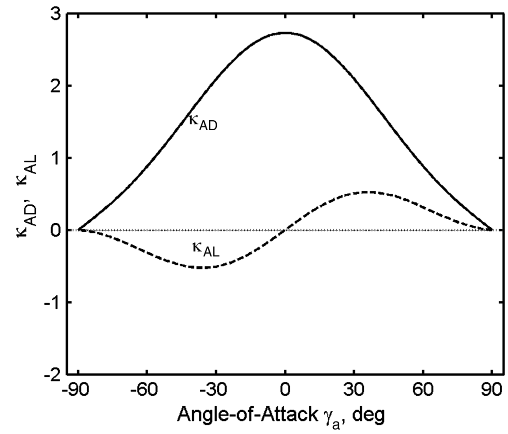


**Fig. 4 Drag and lift coefficients vs angle of attack for a flat plate in hyperthermal free-molecular flow with $\eta_n = \eta_t = 0.7$ and $v_w/v = 0.05$ [24].**

$$v_w = \sqrt{\frac{\pi\Gamma T}{2}} \tag{23}$$

where $\Gamma$ is the specific gas constant and $T$ is the surface temperature of the plate. Setting $T$ to the local atmospheric temperature and using circular LEO velocities yields characteristic values for $v_w/v$ of roughly 0.05. Figure 4 plots Eqs. (22) and (21) over angle of attack for these sample conditions. Positive lift is associated with $\cos(\hat{\boldsymbol{F}}_{\mathrm{AL}} \cdot \hat{\boldsymbol{r}}) > 0$. Both coefficients go to zero at $\hat{\boldsymbol{v}} \perp \boldsymbol{b}_3$, the equilibrium attitude. At $\hat{\boldsymbol{v}} \perp \boldsymbol{b}_3$ there is no lift, and drag is maximized, especially since the full square area is leading.

Aerodynamic accelerations scale with the critical ratio of $A_C/m$:

$$a_{\mathrm{AD}} = \frac{1}{2}\kappa_{\mathrm{AD}}\frac{A_C}{m}\rho_A v^2 = \frac{\kappa_{\mathrm{AD}}\kappa_C}{2\kappa_V \rho}\rho_A v^2 \lambda^{-1} \tag{24}$$

### B. Micrometeoroid Collisions

The solar system is populated by small dust and meteoroid particles orbiting the sun and planets. As these particles collide with a body, they impart momentum, similar to the mechanism of aerodynamic forces. The force associated with these impacts can be modeled by [16]

$$\boldsymbol{F}_P = \dot{m}_P A_C \boldsymbol{v}_{\mathrm{PC}} \tag{25}$$

where $\dot{m}_P$ is the mass flux rate of particles with velocity $\boldsymbol{v}_{\mathrm{PC}}$ relative to the impacted body. Near Earth, the mean particle velocity is roughly directed Earthward:

$$\boldsymbol{v}_{\mathrm{PC}} = G_P \times 20\left[\frac{\mathrm{km}}{\mathrm{s}}\right](-\hat{\boldsymbol{r}}_E) \tag{26}$$

and is a function of the gravitational defocusing factor $G_P$: [20,27]

$$G_P = 0.57 + 0.43\frac{R_E}{r_E} \tag{27}$$

where $R_E$ is the radius of the Earth.

### C. Solar Wind

The sun ejects ionized protons and electrons from its upper atmosphere. Like micrometeoroids, these particles impart energy and momentum when they impact a body. This interaction can be modeled with an effective momentum flux $\dot{p}_{\mathrm{SW}}$, taken as a constant value at a given reference distance from the sun $r_0$. The effective momentum flux at a position $r_s$ is then estimated with an inverse square law [16]:

$$\boldsymbol{F}_{\mathrm{SW}} = \dot{p}_{\mathrm{SW}}\left(\frac{r_0}{r_s}\right)^2 A_c \hat{\boldsymbol{r}}_s \tag{28}$$

Most of these particles are rejected by Earth's magnetopause, so $\dot{p}_{\mathrm{SW}}$ can be thought to represent an upper-limit in the near-Earth environment [28].

## V. Radiation

Photons have both energy and momentum, both of which are related to wavelength. When a photon is absorbed or reflected, momentum is exchanged. The sources of photons considered here include solar radiation, planetary albedo reflection, and thermal radiation. These can be modeled as pressures, whose resultant force is a function of the exposed area $A_c$ and the surface characteristics, which determine how the incoming photons are specularly reflected, diffusely reflected, or absorbed. The dimensionless fractions $\eta_{\mathrm{sr}}$, $\eta_{\mathrm{dr}}$, and $\eta_{\mathrm{ab}}$ account for each of these respective effects for a given wavelength, $\eta_{\mathrm{sr}} + \eta_{\mathrm{dr}} + \eta_{\mathrm{ab}} = 1$. Accelerations associated with radiation scale with the familiar ratio $A_c/m$.

For a radiation pressure $\boldsymbol{P}$, the force acting on a sphere is [20]

$$\boldsymbol{F} = A_C\left[1 + \frac{4}{9}\eta_{\mathrm{dr}}\right]\boldsymbol{P} \tag{29}$$

and for a flat surface with normal $\hat{\boldsymbol{n}}$ as illustrated in Fig. 5 [20]

$$\boldsymbol{F}_S = PA_C(\hat{\boldsymbol{P}}\cdot\hat{\boldsymbol{n}})\left[\left(2\eta_{\mathrm{sr}}(\hat{\boldsymbol{P}}\cdot\hat{\boldsymbol{n}}) + \frac{2}{3}\eta_{\mathrm{dr}}\right)\hat{\boldsymbol{n}} + (\eta_{\mathrm{ab}} + \eta_{\mathrm{dr}})\hat{\boldsymbol{P}}\right] \tag{30}$$

For the sake of added intuition, this analysis assumes that a cube experiences radiation forces similar to those that a sphere experiences [given Eq. (29)], and adopts a simple specular reflection model for the flat plate, taking $\cos\gamma_s = (\hat{\boldsymbol{P}}\cdot\hat{\boldsymbol{n}})$ as the pitch angle [29]:

$$\boldsymbol{F}_S = 2\eta_S PA_C \cos^2\gamma_s \hat{\boldsymbol{n}} \tag{31}$$

Here, the surface properties are captured in the single coefficient $\eta_S$. The direction of these accelerations acting on a plate is a function of the orientation of the surface-normal vector. Thus the orbital and attitude dynamics can be highly coupled. The force acts at an effective center of pressure. As before, any nonzero $\boldsymbol{\delta}_{\mathrm{CP}}$ produces a torque according to Eq. (12), resulting in an angular acceleration that scales with $\lambda^{-2}$.

### A. Solar Radiation Pressure

Photon flux originating from the sun produces an effective pressure $\boldsymbol{P}_{\mathrm{SRP}}$ that can be modeled by [29]

$$\boldsymbol{P}_{\mathrm{SRP}} = \frac{W_0}{c}\left(\frac{r_0}{r_s}\right)^2 \hat{\boldsymbol{r}}_s \tag{32}$$

where $c$ is the speed of light, $W_0$ is the energy flux from the sun taken at a reference distance $r_0$.

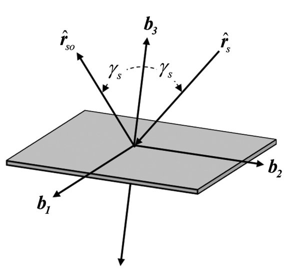


**Fig. 5 Pitch angle and relevant vectors associated with solar radiation pressure.**

### B. Planetary Albedo

Solar flux is also reflected from planets or moons in the solar system. A body orbiting a reflective planet experiences these photons as a secondary pressure originating from the planet's center. Blanco and McCuskey give a model that estimates a maximum radiation pressure from a diffusely reflecting planet at a distance $r_p$ [30]:

$$\boldsymbol{P}_{\mathrm{PA}} = P_s\left(\frac{2}{3}\eta_p\frac{R_p^2}{r_p^2}\right)\hat{\boldsymbol{r}}_p \tag{33}$$

where $R_p$ is the planet's radius. The fraction of the incident solar power that is reflected is given by $\eta_p$, the planet's Bond albedo. This value can vary, particularly for planets with dynamic atmospheres.

### C. Planetary Thermal Emission

Energy and momentum are also associated with thermal emission. The Stephan–Boltzmann law gives the thermal power emitted from an area surface element at a temperature $T$ with emissivity $\xi$:

$$\frac{\mathrm{d}E}{\mathrm{d}t} = \sigma\xi T^4\,\mathrm{d}A \tag{34}$$

Secondary bodies near a thermal emitter can intercept this radiated power and experience a pressure. For an emitting planet with radius $R_p$, temperature $T_p$, and emissivity $\xi_p$, the effective pressure on a secondary body varies inversely with distance $r_p$ squared [16]:

$$\boldsymbol{P}_{\mathrm{TE}} = \frac{\sigma\xi_p T_p^4}{c}\left(\frac{R_p}{r_p}\right)^2\hat{\boldsymbol{r}}_p \tag{35}$$

### D. Thermal Emission

If a body is emitting heat, it can experience a force described by the differential equation in terms of surface elements d$A$ [31]:

$$\mathrm{d}\,\boldsymbol{F}_{\mathrm{TE}} = \frac{\sigma\xi T^4}{c}\,\mathrm{d}A \tag{36}$$

Taking the surface to be isothermal, one can integrate Eq. (36) and find that regular shapes experience no net force or torque. However, if the temperature is nonuniform, a net force results opposite the direction of the temperature gradient.

### E. Poynting–Robertson Drag

If thermal radiation is anisotropic in an inertial frame, a secondary effect known as Poynting–Robertson drag results. This effect is associated with the motion of a radiating body. Here, the difference in the Doppler shifts between the thermal energy radiated in the velocity and antivelocity directions produces a force [32]. As a hot body orbits, heat radiated forward (along $\hat{\boldsymbol{v}}$) is blueshifted by the orbital velocity, implying a higher energy level than the radiation associated with a static body. Alternatively, heat that is radiated backwards is redshifted by the orbital velocity. The result of this effect is a force acting in the drag direction ($-\hat{\boldsymbol{v}}$) that removes energy from the orbit. This drag is given by [2]

$$\boldsymbol{F}_{\mathrm{PR}} = -\frac{\sigma\xi T^4}{c^2}A_C\boldsymbol{v} \tag{37}$$

a quantity that is generally small owing to the $c^{-2}$ term.

### F. Yarkovsky Force

The temperature gradient and resultant force for a spinning body is known as the Yarkovsky force [2,33]. The present analysis focuses on nonspinning equilibria, and hence this force is neglected. However, because the Yarkovsky force is a secondary effect resulting from solar illumination, it can never be greater than the force due to solar radiation pressure and can therefore be bounded.

Models for the Yarkovsky force are typically complicated, owing to the force's dependence on a body's spin axis and surface temperature profile (see for example [34]). The spin axis determines the magnitude of the diurnal and seasonal Yarkovsky effects. The temperature profile depends on the body's geometry, illumination, thermal properties (conductivity, emissivity, specific heat) and spin rate [33]. Models often evaluate the length scale of the thermal penetration depth to differentiate between fast spinning and slow spinning models [2]. Because of the specificity of these models and assumptions, it is challenging to estimate the Yarkovsky force's magnitude across unique geometries or make specific statements about length scaling. Broadly speaking, the Yarkovsky force vanishes for both very small and very large objects and has a maximum value when the body's length scale matches the thermal penetration depth [33].

## VI. Magnetic Fields

Magnetic fields in the space environment can affect a spacecraft's orbit and attitude through a variety of mechanisms.

### A. Magnetic Attraction and Repulsion

Magnetic fields are commonly considered in the design of spacecraft attitude subsystems as either actuators (e.g. torque rods) or disturbances. However, magnetic fields can be produced on a spacecraft both intentionally and unintentionally. In both cases, a dipole-field model is generally sufficient for evaluating the force and torque.

The interaction between a spacecraft-fixed and local environmental magnetic field produces a force according to [35]

$$\boldsymbol{F}_M = \nabla(\boldsymbol{M}_{\mathrm{sc}} \cdot \boldsymbol{B}) \tag{38}$$

where $\boldsymbol{M}_{\mathrm{sc}}$ is the magnetic moment of the spacecraft and $\boldsymbol{B}$ is the local environmental magnetic field. For the case of a dipole approximation of the spacecraft and planetary magnetic fields (given dipole moment $\boldsymbol{M}_P$), this equation can be approximated by [36]

$$\begin{aligned}\boldsymbol{F}_M = \frac{3\mu_0}{4\pi r_M^4}[&(\hat{\boldsymbol{r}}_M \times \boldsymbol{M}) \times \boldsymbol{M}_P + (\hat{\boldsymbol{r}}_M \times \boldsymbol{M}_P) \times \boldsymbol{M} \\ &- 2\hat{\boldsymbol{r}}_M(\boldsymbol{M} \cdot \boldsymbol{M}_P) + 5\hat{\boldsymbol{r}}_M((\hat{\boldsymbol{r}}_M \times \boldsymbol{M}) \cdot (\hat{\boldsymbol{r}}_M \times \boldsymbol{M}_P))]\end{aligned} \tag{39}$$

where $\mu_0$ is the permeability of free space and $\boldsymbol{r}_M$ is the vector separating the planet and spacecraft centers. Experience suggests that this force tends to be negligibly small, even for powerful magnets located at the Earth's surface. However, the torque applied between the two magnetic fields can be significant [20]:

$$\boldsymbol{\tau}_M = \boldsymbol{M}_{\mathrm{sc}} \times \boldsymbol{B} \tag{40}$$

This "compass torque" is the magnetic effect that is most often an issue for spacecraft.

For a permanent magnet, the magnetic moment is a function of the geometry and magnetization $\boldsymbol{\Omega}$, the dipole moment strength per unit volume, roughly [37]

$$\boldsymbol{M}_{\mathrm{sc}} = \kappa_V \lambda^3 \boldsymbol{\Omega} \tag{41}$$

The direction of magnetization points from the magnet's south pole to north pole. The magnetic dipole moment of a permanent magnet goes with $\lambda^3$. Dividing this torque by inertia as in Eq. (11), one finds that angular acceleration due to magnetic torques is proportional to $\lambda^{-2}$.

For an electromagnet with $n_M$ coils of conductor with current $i$, the dipole moment is given by [38]

$$\boldsymbol{M}_{\mathrm{sc}} = \oint i \,\mathrm{d}A = n_M i A \tag{42}$$

where $A$ is the area effectively enclosed by each coil, e.g. $A_C$. Electrical resistance $\chi$ is the product of the conductor's material resistivity $\sigma_M$ and the ratio of the conductor's length $l_M$ to its cross-sectional area $A_M$ [37]:

$$\chi = \sigma_M \frac{l_M}{A_M} \tag{43}$$

As the current or number of coils increases, a larger conductor cross section is required to maintain the same $i^2\chi$ power losses. Consequently, the dipole magnetic moment of an electromagnet goes also with $\lambda^3$ [37]. The magnetization model in Eq. (41) can therefore be applied to both permanent magnets and current-carrying coils. Table 3 gives an estimate for the magnetization of three cases: a rare Earth permanent magnet, a nonspinning spacecraft with an unintentional residual magnetic field, and commercially available magnetic torquers. According to this model, magnetic orbital acceleration is length-independent, and angular acceleration scales with $\lambda^{-2}$.

### B. Eddy Current Damping

A conductive body moving through a magnetic field experiences a damping effect associated with eddy currents. The changing magnetic field within the conductor drives electrons, which set up current loops. Resistance in the material dissipates these currents as heat, removing energy from the system. The net effect is a force and torque opposite the direction of motion.

Accurately modeling eddy currents is challenging [38]. As in the case of magnetic attractive and repulsive forces, the magnitude of the eddy current force is exceedingly small. Eddy current torque, however, can significantly affect spacecraft attitude [40]:

$$\boldsymbol{\tau}_{\mathrm{EC}} = -\varepsilon_{\mathrm{EC}} \boldsymbol{B} \times (\boldsymbol{\omega} \times \boldsymbol{B}) \tag{44}$$

The torque is a source of damping because it opposes angular velocity. The constant $\varepsilon_{\mathrm{EC}}$ is associated with the body's geometry and resistivity [40]:

$$\varepsilon_{\mathrm{EC}} = \frac{\kappa_{\mathrm{EC}}}{\sigma}\lambda^5 \tag{45}$$

Expressions for $\varepsilon_{\mathrm{EC}}$ have been calculated for thin-shell spheres and cylinders, as well as a circular loop of wire. Here, the sphere and cube are both treated as thin-shelled spheres with thickness $\kappa_\varepsilon \lambda$, while the plate is treated as a circle of wire. The corresponding coefficients $\kappa_{\mathrm{EC}}$ are given in Table 4. Dividing eddy current torque by inertia as in Eq. (11), one finds that the resultant angular acceleration is length-independent [42].

Though this analysis focuses on nonspinning equilibria, eddy current damping is included in an effort to understand the magnitude of damping accelerations that can act during motion transients.

### C. Lorentz Force

A charged body with a velocity relative to a magnetic field experiences the Lorentz force. Here, electrostatic charge can transfer orbital energy and momentum to and from a planet through its corotating magnetic field via the Lorentz force. The Lorentz force $\boldsymbol{F}_{\mathrm{LZ}}$ acting on an orbiting body with electrostatic charge $q$ is [43,44]

**Table 3 Magnetization estimates**

| Source | $\Omega$, A/m | Reference |
|---|---|---|
| Rare earth permanent magnets | $8 \times 10^5$ | [39] |
| $\Omega_R$, unintentional residual spacecraft magnetization | 0.1–1.0 | [40] |
| $\Omega_T$, magnetic torquers | 200–6400 | [41] |

**Table 4 Dimensionless scale factors for magnetic accelerations**

| Scale factor | Sphere [42] | Cube [42,45,46] | Thin square plate [40,46] |
|---|---|---|---|
| $\kappa_{\mathrm{EC}}$ | $\frac{\pi}{24}\kappa_\varepsilon$ | $\frac{\pi}{24}\kappa_\varepsilon$ | $\frac{\pi}{32}\kappa_{\mathrm{CS}}$ |
| $\kappa_{\mathrm{CAP}}$ | 0.5 | 0.66 | 0.36 |

$$\boldsymbol{F}_{\mathrm{LZ}} = q\boldsymbol{v}_B \times \boldsymbol{B} \tag{46}$$

where $\boldsymbol{v}_B$ is the velocity relative to a magnetic field $\boldsymbol{B}$. For a magnetic field rotating with an angular velocity $\boldsymbol{\omega}_B$ the relative velocity is [44]

$$\boldsymbol{v}_B = \boldsymbol{v} - \boldsymbol{\omega}_B \times \boldsymbol{r}_B \tag{47}$$

where $\boldsymbol{r}_B$ is the body's position with respect to the magnetic field's center, usually taken to be a planet's center of mass. The direction of this force is dictated by the body's orbit and the local magnetic field; $q$ can only modulate the force's magnitude along this direction. Figure 6 illustrates a sample equatorial, retrograde, elliptical orbit around Earth. The arrows indicate the direction and relative magnitude of the Lorentz force at various positions for a positively charged body. The force is largest at perigee, where the body's velocity and the local magnetic field are both maximized. The force can do work on the body's orbit at positions where $\boldsymbol{F}_{\mathrm{LZ}}$ has a component along $\hat{\boldsymbol{v}}$.

The associated Lorentz acceleration scales with $q/m$, the charge-to-mass ratio:

$$\boldsymbol{a}_{\mathrm{LZ}} = \frac{q}{m}\boldsymbol{v}_r \times \boldsymbol{B} \tag{48}$$

This ratio is a function of the body's geometry, electrostatic potential, and the local space plasma environment. For a desired charge to be established, a biased electric potential $\phi$ must be generated on a body with sufficiently large self-capacitance $C$:

$$q = C\phi \tag{49}$$

In a vacuum, self-capacitance is a function of geometry only. The three geometries of interest have capacitance expressions that take the form [45,46]

$$C = \kappa_{\mathrm{CAP}} 4\pi\varepsilon_0 \lambda \tag{50}$$

where $\varepsilon_0$ is the permittivity of free space and $\kappa_{\mathrm{CAP}}$ is a dimensionless coefficient given in Table 4 for each shape. These models suggest that $q/m$ and the consequent Lorentz acceleration scales with $\lambda^{-2}$:

$$\frac{q}{m} = \frac{4\pi\varepsilon_0\kappa_{\mathrm{CAP}}}{\kappa_V \rho}\phi\lambda^{-2} \tag{51}$$

The environment around a planetary magnetic field generally consists of rarefied plasma whose presence increases the effective self-capacitance. As a result, these values can be treated as lower bounds.

The Lorentz force acts at a body's effective center-of-charge $\boldsymbol{\delta}_q$. The force therefore applies a torque of the form in Eq. (12) when the center of mass and center-of-charge are not collocated. This torque has been proposed as an attitude actuator for spacecraft capable of controllable charges [47]. For the regular geometries presented here,

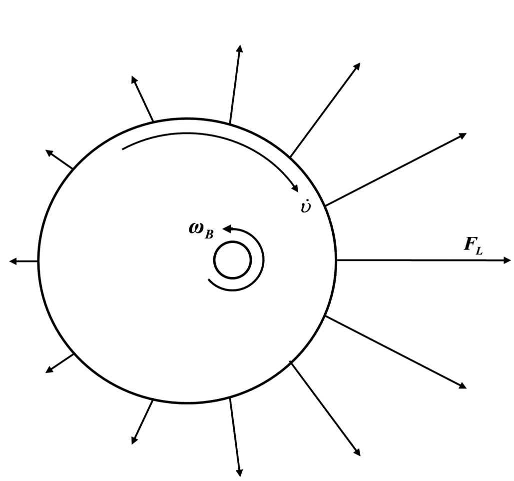


**Fig. 6 Direction of Lorentz force throughout a retrograde elliptical Earth orbit for $q > 0$.**

**Table 5 Acceleration dependence on λ and geometric scale factors**

| Source | Orbital | Angular |
|---|---|---|
| Gravity | $\kappa_V \lambda^0$ | $\kappa_I \lambda^0$ |
| Particle collisions | | |
| Aerodynamic forces | $\frac{\kappa_{\mathrm{AD}}\kappa_C}{\kappa_V}\lambda^{-1}$ | $\frac{\kappa_{\mathrm{AD}}\kappa_C}{\kappa_I}\lambda^{-2}$ |
| Solar wind micrometeoroid collisions | $\frac{\kappa_C}{\kappa_V}\lambda^{-1}$ | $\frac{\kappa_C}{\kappa_I}\lambda^{-2}$ |
| Radiation | | |
| Solar radiation pressure planetary albedo thermal emission | $\frac{\kappa_C}{\kappa_V}\lambda^{-1}$ | $\frac{\kappa_C}{\kappa_I}\lambda^{-2}$ |
| Poynting–Robertson drag | $\frac{\kappa_C}{\kappa_V}\lambda^{-1}$ | —— |
| Magnetic fields | | |
| Magnetic attraction (dipole interactions) | $\kappa_V \lambda^0$ | $\frac{\kappa_V}{\kappa_I}\lambda^{-2}$ |
| Eddy current damping | —— | $\frac{\kappa_{\mathrm{EC}}}{\kappa_I}\lambda^0$ |
| Lorentz force (vacuum environment) | $\frac{\kappa_{\mathrm{CAP}}}{\kappa_V}\lambda^{-2}$ | $\frac{\kappa_{\mathrm{CAP}}}{\kappa_I}\lambda^{-3}$ |

$\boldsymbol{\delta}_q = 0$. However, an arbitrarily small deviation in the local charge distribution will produce a torque of the form in Eq. (12). In a vacuum environment, the resulting angular acceleration scales with $\lambda^{-3}$.

## VII. Simulation Results

The acceleration scaling from the preceding models are summarized in Table 5. Here, the magnitude of each acceleration is presented along with the appropriate scale factors. With the exception of gravitational accelerations, magnetic attraction, and eddy current damping, each acceleration is somehow dependent on λ. In each case, the accelerations increase in magnitude as λ decreases.

Simulations are used to associate these scaling laws with realistic values for the near-Earth environment. The simulations use the Earth Gravity Model (EGM96) [48] and the International Geomagnetic Reference Field (IGRF95) [49]. For altitudes below 1000 km, the 1976 Standard Atmosphere Model [50] is used. For altitudes greater than 1000 km, density data from C. W. Allen's Astrophysical Quantities [51] is used. Tables 6 and 7 give the environmental and spacecraft-specific constants used in the simulations, as well as their references. The spacecraft density is taken to be 79 $\mathrm{kg/m^3}$, the rule-of-thumb density for typical spacecraft [54]. The reflective efficiency $\eta$ is taken to be characteristic of a very reflective surface [29]. Two magnetic fields are considered, residual and intentional, denoted by the magnetization terms $\Omega_R$ and $\Omega_T$ respectively. The conductivity $\sigma_{\mathrm{EC}}$ is taken to be characteristic of gold traces. The Lorentz force is evaluated for a spacecraft in a retrograde orbit, such that $\boldsymbol{v}_B$ is maximized.

Table 8 is the legend for Figs. 7–14. These figures give the magnitude of each of the 14 modeled accelerations as a function of λ. The accelerations are normalized by the magnitude of Earth's point-mass attraction and plotted on a log-log scale. Figure 7 shows each acceleration at altitudes of 500, 1000, and 10,000 km. The accelerations are unscaled in that each of the unitless scale factors $\kappa_i$ (with the exception of $\kappa_\varepsilon$) in Table 5 is set to unity. These plots can be used to provide results specific to any shape of interest. For a given shape and orbit, the plots identify which accelerations must be included and which accelerations can justifiably be neglected for an accurate analysis. Alternatively, these plots identify particular accelerations and altitudes that offer a predominant environmental

**Table 6 Environmental constants used in simulations**

| Parameter | Value | Reference |
|---|---|---|
| $\dot{m}_P$ | $6.13 \times 10^{-16}\ \mathrm{kg/m^2 s}$ | [16,27] |
| $\eta_p$ | 0.306 | [52] |
| $\dot{p}_{\mathrm{SW}}$ | $2.3 \times 10^{-9}\ \mathrm{kg/m\,s^2}$ | [28] |
| $r_0$ | 1 AU | [23] |
| $T_p$ | 255 K | [53] |
| $W_0$ | $1368\ \mathrm{J/m^2\,s}$ | [23] |
| $\xi_p$ | 1 | —— |

**Table 7 Spacecraft constants used in simulations**

| Parameter | Value | Reference |
|---|---|---|
| $\eta$ | 0.85 | [29] |
| $\eta_{ab}$ | 0.1 | —— |
| $\eta_{dr}$ | 0.1 | —— |
| $\eta_n$ | 0.70 | [24] |
| $\eta_t$ | 0.70 | [24] |
| $\kappa_\varepsilon$ | 0.0025 | —— |
| $\Omega_R$ | 0.5 A/m | Table 3 |
| $\Omega_T$ | 1000 A/m | Table 3 |
| $\omega$ | 0.1 rad/s | —— |
| $\rho$ | 79 kg/m$^3$ | [54] |
| $\sigma_{EC}$ | $4.2 \times 10^7$ (ohm-m)$^{-1}$ | [55] |
| $\xi$ | 0.85 | —— |
| $\phi$ | 1000 V | —— |

acceleration, and therefore an opportunity for possible propellantless propulsion.

Figure 8 gives the scaled accelerations for the three geometries of interest in this analysis. These figures include accelerations due to solar pressure, aerodynamic drag, and the Lorentz force. Each can dominate the nongravitational dynamics at particular length scales and altitudes. Aerodynamic drag, for example, is the largest acceleration at 500 km, while solar pressure is largest at 10,000 km. With a $\lambda^{-3}$ dependence, the Lorentz force becomes the largest as the characteristic length approaches the submillimeter scale. Figure 8 suggests that the plate geometry, when aligned for maximum area, experiences the largest effects from nongravitational accelerations, owing to its high $A/m$ ratio: $\kappa_C/\kappa_V$.

Finally, Fig. 9 shows the regions of altitude and length scale within which each orbital acceleration dominates for the choices of geometry. The cube and sphere share a nearly identical map that is mostly dominated by acceleration due to Earth oblateness. For the plate geometry, oblateness dominates large scales, while small scales are divided between solar radiation pressure at high altitudes (>600 km) and atmospheric drag at lower altitudes. The dashed line shows the altitude of geostationary orbit (35,786 km) for reference.

Simulations are also used to find the relative magnitudes of angular accelerations. Here, the environmental torques are modeled for the near-Earth environment. Except for gravity gradient, magnetism, and eddy current torques, all of the environmental torques are a product of an environmental force along a line of action offset from the body's mass center. That is, these torque models take the form of Eq. (12), where $\boldsymbol{\delta}$ is taken to be the offset from the mass center. This analysis focuses on the maximum relative magnitude a torque achieves. To this end, Eq. (13) is used with $\kappa_T$ taken to be a constant, implying that the offset $\boldsymbol{\delta}$ varies with size. For example, given $\kappa_T = 0.01$, the torques' moment-arm is 1% of the characteristic length. This assumption may best model manufacturing errors. Two magnetic torques are considered: disturbance torques associated with unintentional residual fields (denoted MR) and actuator torques associated with a magnetic torquer (denoted MT). Many of the forces or torques are dependent on $A_C$. These tend to rotate the plate about a minor axis since the area perpendicular to the major axis $\boldsymbol{b}_3$ is negligible. The simulations therefore use the minor moment of inertia.

Figure 10 shows the unscaled ($\kappa_i = 1$) angular accelerations as a function of characteristic length at altitudes of 500, 1000, and 10,000 km. Eddy-current damping accelerations for $\omega = 0.1$ rad/s are length-independent and relatively large. This suggests that any rotational dynamics will damp out relatively quickly. Gravity-gradient accelerations, here due to a displacement of the mass center by $\boldsymbol{\delta}$, are also length-independent. Of the accelerations that scale with $\lambda$, magnetic actuators predictably dominate; after all, this simulation models the entire unscaled body as a single magnetic torquer. As in the orbital acceleration case, the relative importance of the remaining accelerations can depend on altitude.

Figure 11 shows the dominant accelerations applied to sphere, cube, and plate geometries. Again, the plate geometry experiences the highest of the nongravitational accelerations. At LEO altitudes, aerodynamic drag can dominate the angular accelerations for small bodies. At higher altitudes, solar pressure and residual magnetic interactions become increasingly important. The Lorentz force, despite having a $\lambda^{-3}$ dependence, does not overcome these accelerations until submillimeter scales.

Finally, Fig. 12 shows the regions of altitude and length scale within which each angular acceleration dominates for the geometry choices. The cube and sphere share a nearly identical map, which differs from the map for the plate geometry mostly in terms of the Lorentz force. For the sphere and cube, the Lorentz force can dominate the accelerations at very small length scales. Roughly speaking, gravity gradient dominates large bodies ($\lambda > 1$ m), while small bodies are dominated by solar radiation pressure at high altitudes (>600 km) and atmospheric drag at lower altitudes.

Figure 12 also suggests what the passive equilibrium attitude for a body is if a control actuator is absent. In the solar pressure dominated regime, the body will tend to align such that the center of solar radiation pressure is "downwind" of the center of mass. Likewise, bodies in the aerodynamic drag dominated region will align such that the center of aerodynamic pressure is downwind of the center of mass. Finally, those bodies in the gravity gradient dominated region will align with familiar radially aligned equilibrium.

Figure 13 augments Fig. 12 with a set of contour lines that display the actuator torque required to overcome the locally dominant environmental accelerations. Previous figures already suggest that magnetic torquers can provide these magnitudes of torque at every length scale given a typical dipole moment. This figure helps to size other actuators.

Previous studies [10,11] have introduced a prototype IC spacecraft-on-chip architecture intended to demonstrate functionality at small $\lambda$. The design consists of a silicon plate ($\rho$= 2300 kg/m$^3$) with $\lambda = 1$ cm and $\kappa_\varepsilon = 0.0025$. Taking $\boldsymbol{\delta} = 1$ mm, Fig. 14 shows simulations of this architecture in the near-Earth environment. Each of the variables is plotted as a function of altitude. Further simulation results and details of this sample architecture are given in Sec. VIII.

**Table 8 Acceleration legend for Figs. 7–14**

| Initials | Acceleration |
|---|---|
| AD | Aerodynamic drag |
| EC | Eddy current drag |
| GG | Gravity gradient |
| GR | General relativity |
| LZ | Lorentz force |
| M | Magnetism |
| MT | Magnetism: torquer |
| MR | Magnetism: residual field |
| Moon | Lunar gravity |
| OB | Earth oblateness |
| PA | Planetary albedo |
| PC | Particle collisions |
| PL | Solar system planetary gravity |
| PR | Poynting–Robertson drag |
| SP | Solar pressure |
| SR | Special relativity |
| SW | Solar wind |
| Sun | Solar gravity |

## VIII. Discussion

These results have implications for small-spacecraft design, though there are obvious limits in their interpretation. Specifically, constant spacecraft density likely does not apply across all length scales. It also may not be realistic to model a plate as having a constant $\kappa_\varepsilon$ across all $\lambda$. Despite these limitations, this analysis inspires relevant applications. The candidate spacecraft-on-chip used in the preceding analysis is designed with a 1 cm characteristic length in order to enable new mission opportunities based on nongravitational accelerations. This discussion briefly considers three such

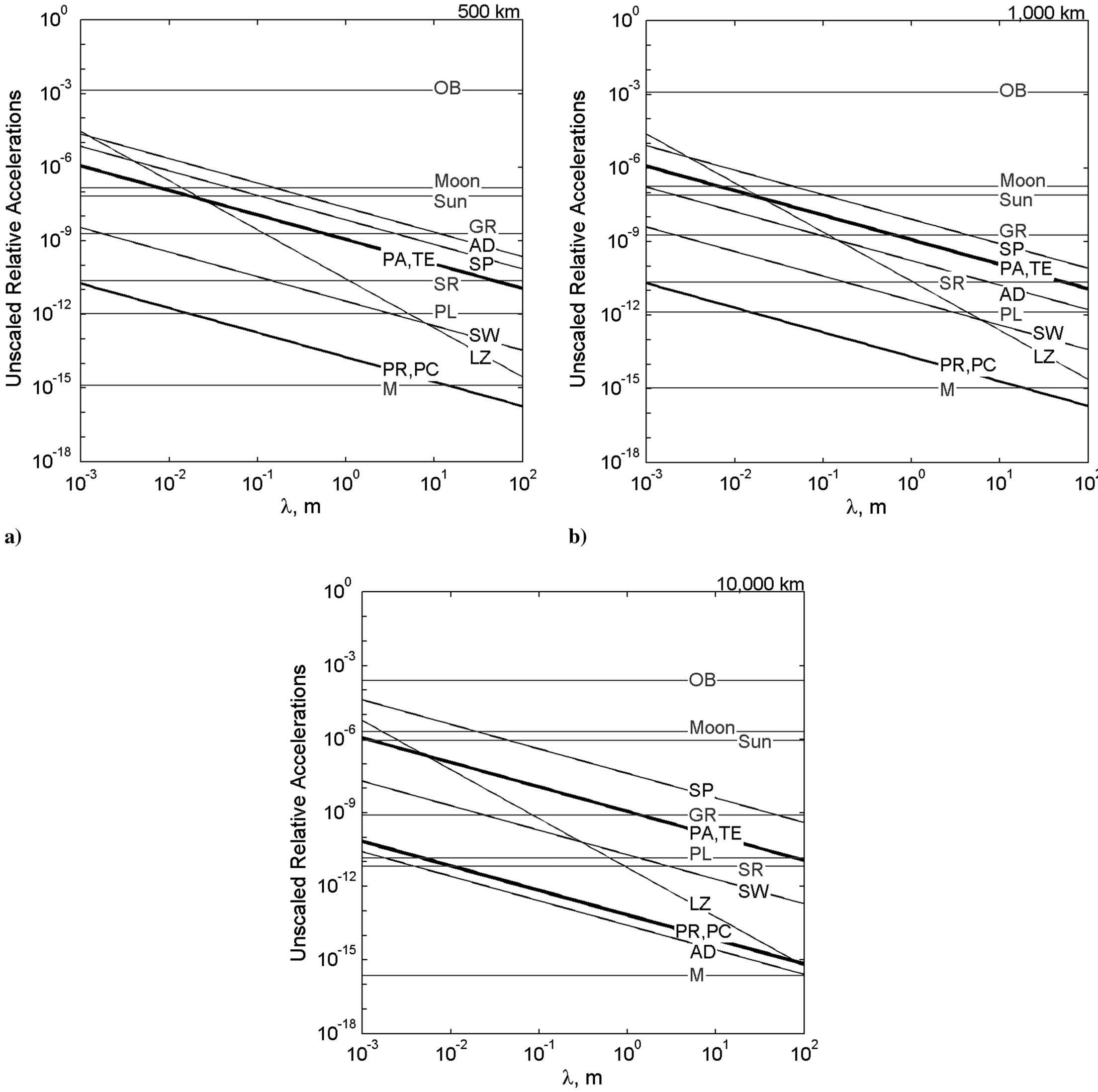


c)

**Fig. 7 Unscaled orbital accelerations at a) 500, b) 1000, and c) 10,000 km altitude as a function of characteristic length, normalized to Earth's two-body gravity.**

opportunities for the candidate bus: solar sailing, aerodynamic reentry, and Lorentz propulsion.

### A. Solar Sail

A solar sail exploits solar radiation pressure as a means of propellantless propulsion. This analysis suggests that useful solar pressure can be achieved with small, thin platelike structures. In fact, solar sail architectures benefit from small size in other ways as well. Typical sail designs are extremely large and challenging to construct, deploy, and actuate. Greschik [56] suggests that dimensional challenges are primarily responsible for the as yet unsuccessful solar sail tests, despite 30 years of attempts. The range of magnitudes involved in solar sails make structural analyses intractable, fabrication demanding, and ground testing extremely challenging. These issues have motivated the development of smaller architectures including solar kites [57], microsolar sails [58], and nanosails [59].

For interplanetary dust, solar radiation pressure can exceed gravity. Here, the critical radius of a particle is roughly a tenth of a micron, below which the particle can be too small to absorb or reflect the photon [10]. Highly reflective interplanetary dust particles of this size can escape solar gravity if released from a comet near the sun [2]. These so-called $\beta$ meteoroids were most recently detected by the Ulysses [60] and Galileo [61] spacecraft.

This analysis indicates that the candidate spacecraft-on-chip architecture can capitalize on length scaling to achieve significant solar pressure acceleration. That is, the bus itself, by virtue of its geometry, behaves as a solar sail. The millimeter-scale design can be fabricated using IC techniques and can be readily tested in a 1 G environment. Further, by capitalizing on natural dynamics, it may be capable of avoiding the nontrivial challenges associated with solar sail control and actuation. Previous research [10] has evaluated this concept, accounting for passive attitude control mechanisms and proposing sample missions concepts.

A common metric for solar sail designs is the lightness number $\beta_{SP}$, which compares the solar pressure acceleration to solar gravitation [29]:

$$\beta_{SP} \equiv \frac{a_S}{a_G} = 2\frac{W_0 r_0^2}{c\mu\rho}\frac{\eta\kappa_C}{\kappa_V}\lambda^{-1} \tag{52}$$

This metric accurately describes the acceleration's dependence on body size for lengths above the wavelength of visible light. The candidate silicon spacecraft-on-chip bus achieves a lightness number of 0.01, meaning that the magnitude of solar pressure is 1% of solar gravity. Though this value is smaller than many proposed solar sail designs, there are a number of possible applications for it in geocentric, heliocentric, or three-body orbits as explored in previous research [10]. Even thinner bodies retain the advantages of stiffness and ready deployment, and they would better compete with the lightness number of larger sails.

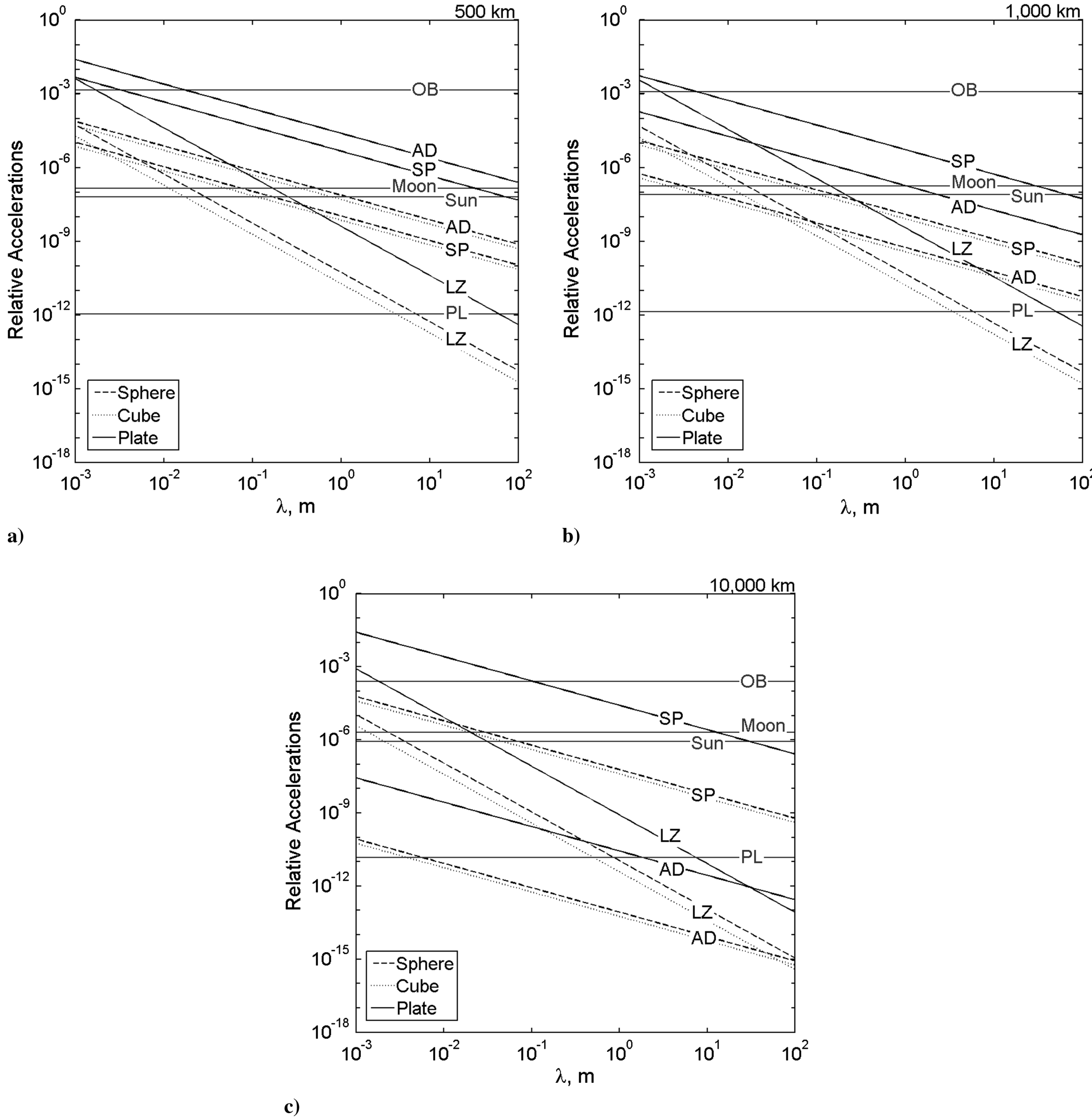


**Fig. 8 Orbital accelerations for a sphere, cube, and plate at a) 500, b) 1000, and c) 10,000 km altitude as a function of characteristic length, normalized to Earth's two-body gravity.**

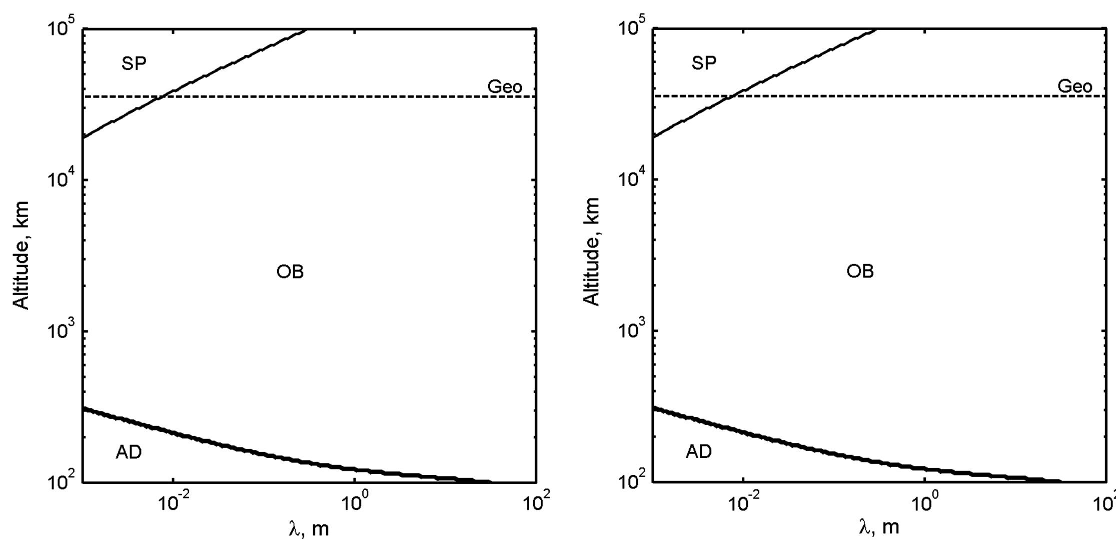


**Fig. 9 Regions of dominant orbital acceleration for a) both a sphere and cube geometry and b) a plate geometry as a function of characteristic length and altitude.**

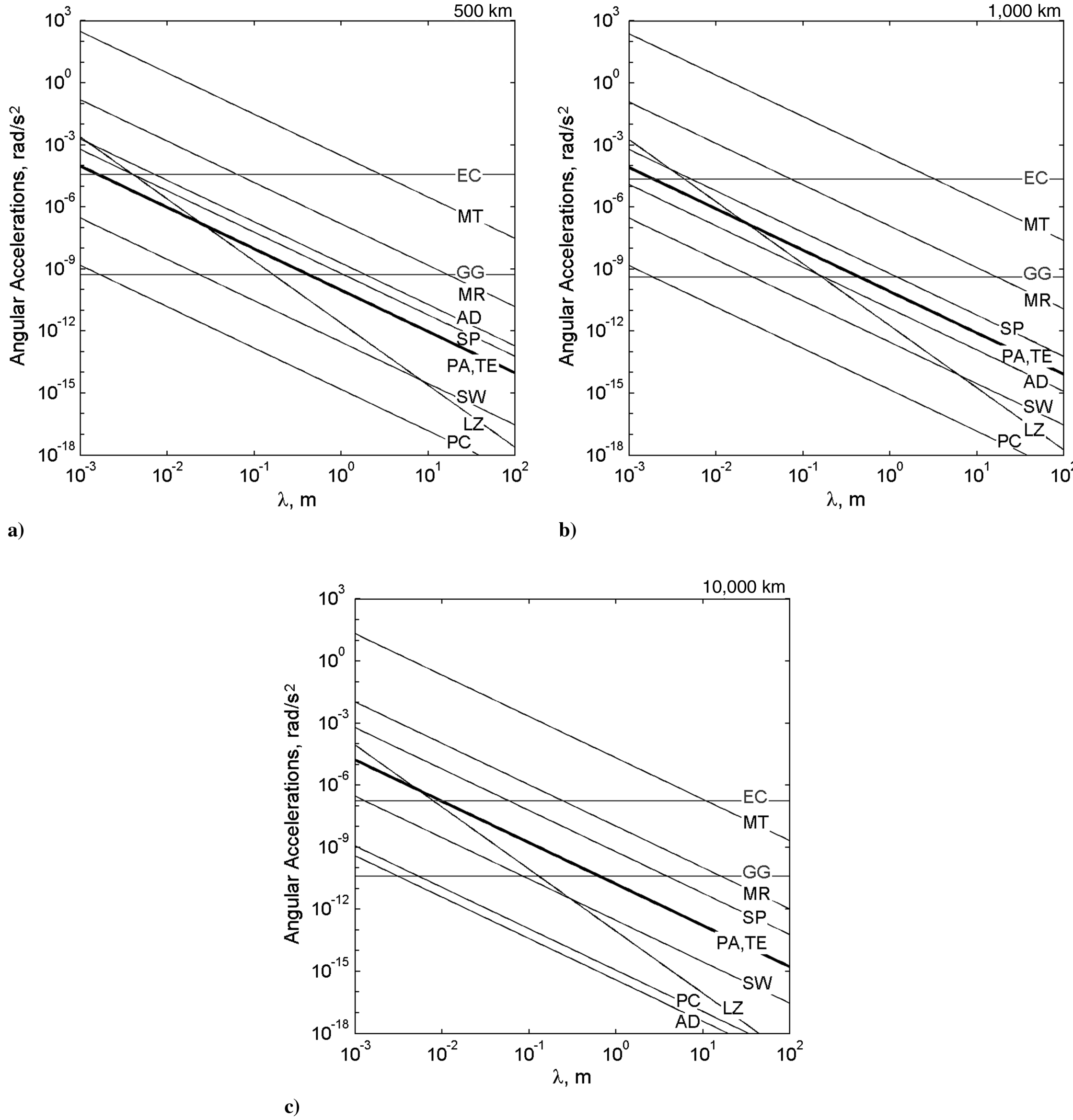


**Fig. 10 Unscaled angular accelerations at a) 500, b) 1000, and c) 10,000 km altitude as a function of characteristic length.**

### B. Reentry Dynamics

Like most of the nongravitational orbital accelerations, atmospheric drag depends on the area-to-mass ratio $A_C/m$. The inverse of this ratio appears in the commonly used ballistic coefficient, defined to be a ratio of inertia to aerodynamic drag [62]:

$$\beta_{\mathrm{AD}} \equiv \frac{m}{\kappa_{\mathrm{AD}} A_C} = \frac{\kappa_V \rho}{\kappa_{\mathrm{AD}} \kappa_C} \lambda \tag{53}$$

This ratio determines a body's drag-limited lifetime in LEO. Low values of $\beta_{\mathrm{AD}}$ correspond to satellites whose orbits are highly affected by atmospheric drag, and consequently deorbit more quickly than bodies with high $\beta_{\mathrm{AD}}$. Typical spacecraft have ballistic coefficients on the order of 10 to 100 $\mathrm{kg/m^2}$ [63]. When face-on to the flow ($\gamma_A = \pi/2$), the candidate spacecraft-on-chip bus has a ballistic coefficient of 0.023 $\mathrm{kg/m^2}$.

Figure 14b shows that acceleration associated with magnetic actuator torque are greater than that associated with atmospheric drag. This feature suggests that a magnetic torquer could align the attitude of a plate with the magnetic field when commanded, enabling a form of controlled aerobraking or reentry.

A primary challenge for spacecraft reentry maneuvers is heat management, where both the rate and total load of heat can cause catastrophic failure. Essentially, aerodynamic drag converts the spacecraft's kinetic energy to thermal energy. A spacecraft must be capable of both decelerating and shedding heat rapidly enough to survive reentry. In their assessment of the survivability of small orbital debris, Koppenwallner et al. [62] developed a model for reentry that explicitly considers λ. Characteristic length enters the model through two of the three aerodynamic similarity parameters: Reynolds number and Knudsen number [62]:

$$Re = \frac{\rho_{\mathrm{AD}} v}{\mu_{\mathrm{AD}}} \lambda \tag{54}$$

$$Kn = \frac{\varsigma}{\lambda} \tag{55}$$

where $\mu_{\mathrm{AD}}$ is the local atmospheric fluid viscosity and $\zeta$ is the mean free path of the atmospheric gases. The third similarity parameter, the Mach number, depends on only velocity and local fluid properties. These three parameters define the flow environment and heat transfer regime of the reentering body. Free-molecular flow is defined by $Kn > 10$, and hypersonic continuum flow is defined by $Kn < 0.1$. Intermediate values are characterized as transitional flow and are approximated with some choice of bridging function. The heat imparted to the reentry body is modeled by [62]

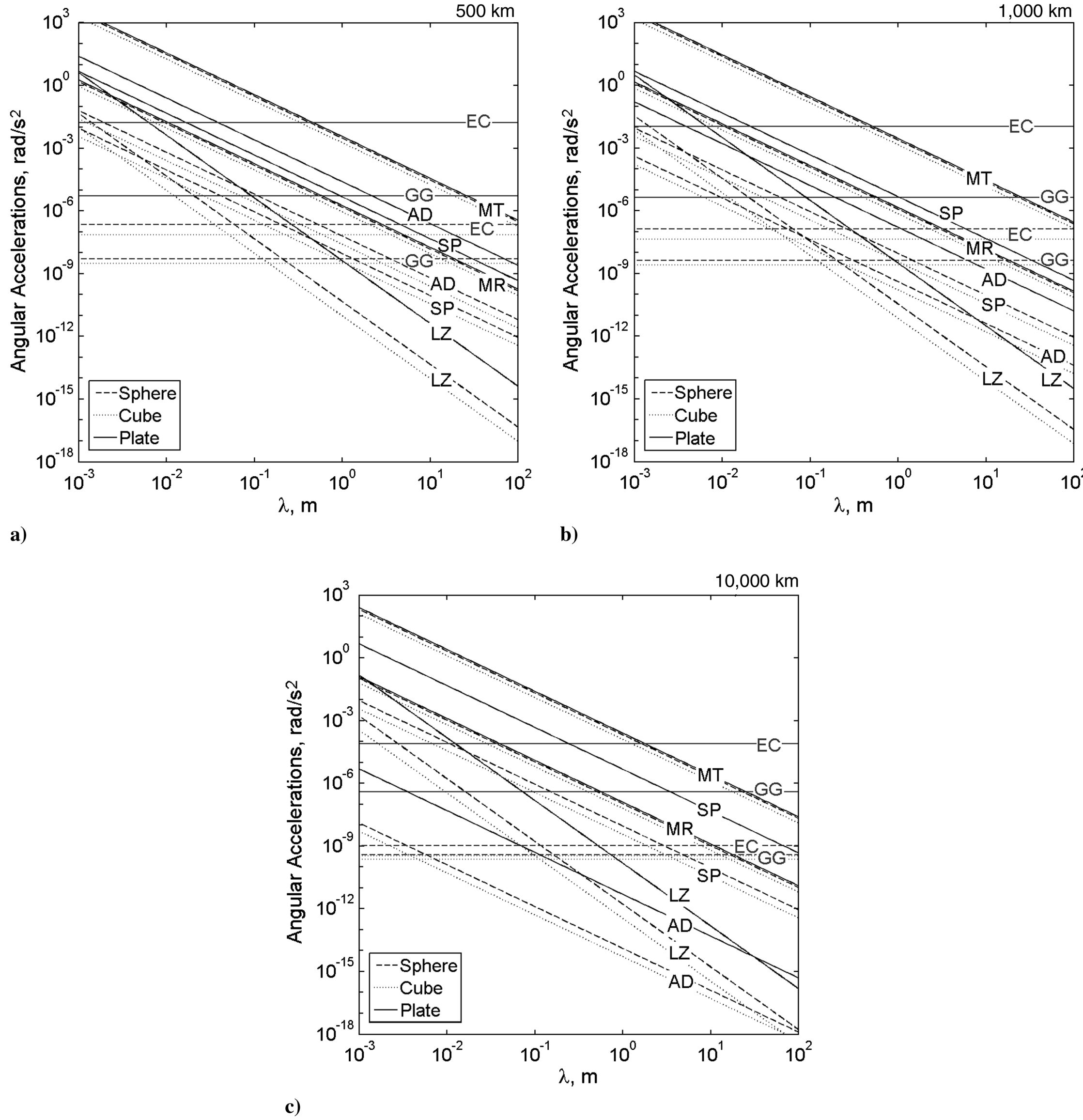


**Fig. 11 Angular accelerations for a sphere, cube, and plate at a) 500, b) 1000, and c) 10,000 km altitude as a function of characteristic length.**

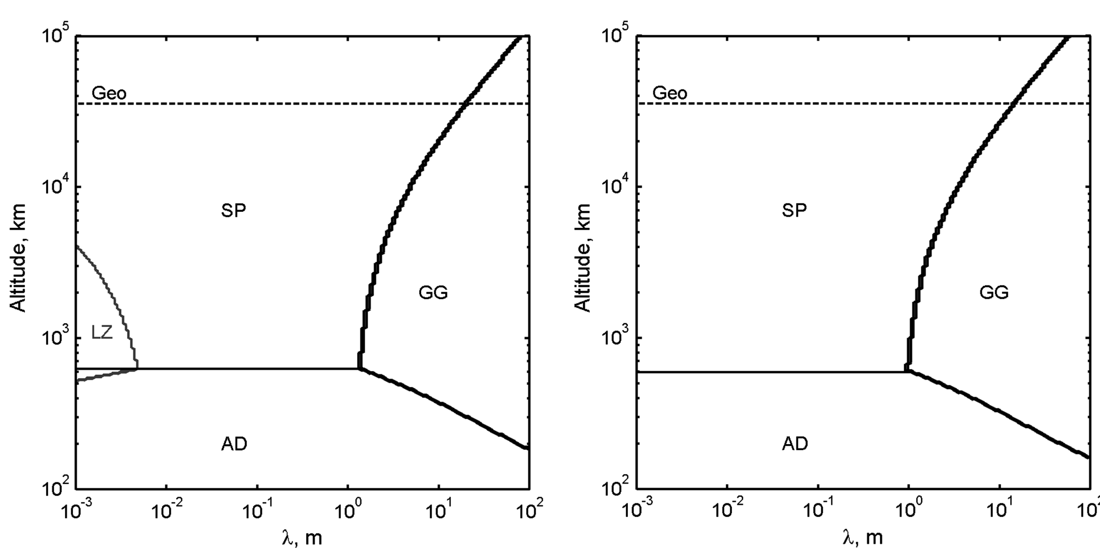


**Fig. 12 Regions of dominant angular acceleration for a) both a sphere and cube geometry and b) a plate geometry as a function of characteristic length and altitude.**

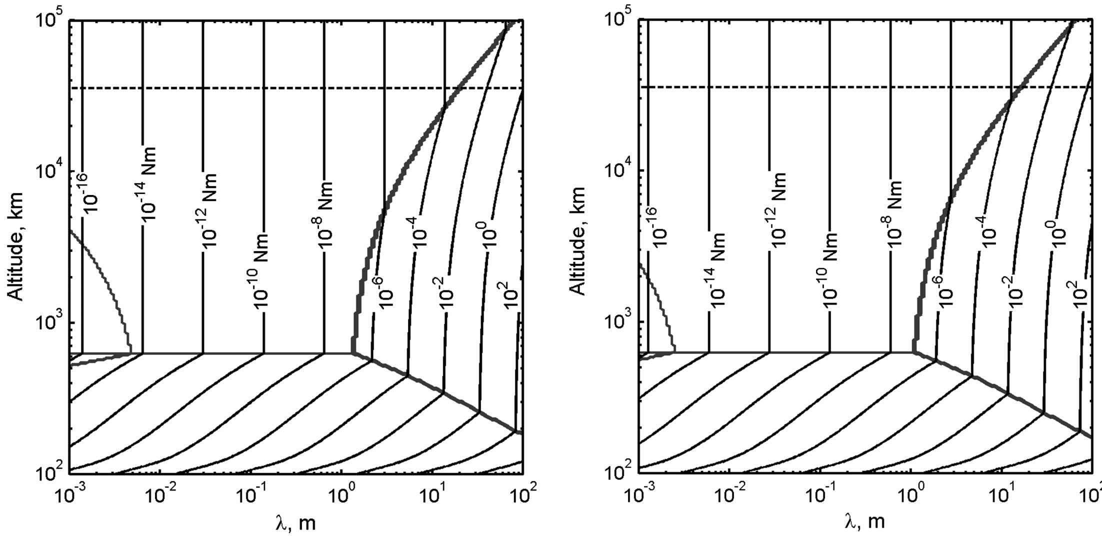


a) b)

**Fig. 13 Torque required to overcome the dominant environmental angular acceleration for a) both a sphere and cube geometry and b) a plate geometry as a function of characteristic length and altitude.**

$$\dot{Q}_{\text{aero}} = \frac{1}{2} St \rho_{\text{AD}} v^3 A_C \tag{56}$$

where the Stanton number $St$ varies according to the flow regime. The heat input is therefore a function of $\lambda^2$ explicitly, with an additional, though less clear, dependence on $\lambda$ through the fluid similarity parameters. Further, the back half of the spacecraft can radiate heat $\dot{Q}_{\text{rad}}$ to and from the surrounding planet (with temperature $T_p$) according to the Stephan–Boltzmann law given by Eq. (34). As before, this radiation term is a function of $\lambda^2$.

Given these models for heat transfer, the temperature of a spacecraft with specific heat capacity $c_p$ follows the first-order differential equation [62]:

$$\dot{T} = \frac{\dot{Q}_{\text{aero}} + \dot{Q}_{\text{rad}}}{m c_p} \tag{57}$$

Thus the ratio of $A/m$ also appears in the heat transfer equation, which suggests that the temperature of small bodies is more sensitive to heat rates. It turns out that dust particles can survive reentry at low temperatures thanks to their small size [6,7]. Aerodynamic drag decelerates the dust particles to subsonic velocities in the upper atmosphere where the density is low and aerothermal heat rates are very low. Each year, thousands of metric tons of small interplanetary dust particles reach the Earth's surface unaffected while larger meteoroids energetically ablate as meteorites [64].

This drag and thermal model was simulated for a proposed spacecraft-on-chip architecture (a square flat plate with $\lambda = 1$ cm and $\kappa_\varepsilon = 0.0025$) from an altitude of 350 km. The results of this simulation are given in Fig. 15. For the first orbit, the thin square plate is kept edge-on to the flow and drag is minimal. Once commanded, the attitude is taken to be face-on to the velocity, such that drag is maximized. The altitude rapidly drops, and the temperature increases to a peak value of only about 105°C during maximum deceleration, after which it settles to a steady state temperature driven by the Earth's thermal radiation. This peak heating occurs in the free-molecular flow regime and results in temperatures low enough to suggest that an IC could operate throughout reentry. There may be meaningful mission opportunities for a small sensor that can sample many altitudes of the atmosphere continuously throughout the reentry process, and one that furthermore would not experience the plasma-related communications dropout of hotter reentering spacecraft.

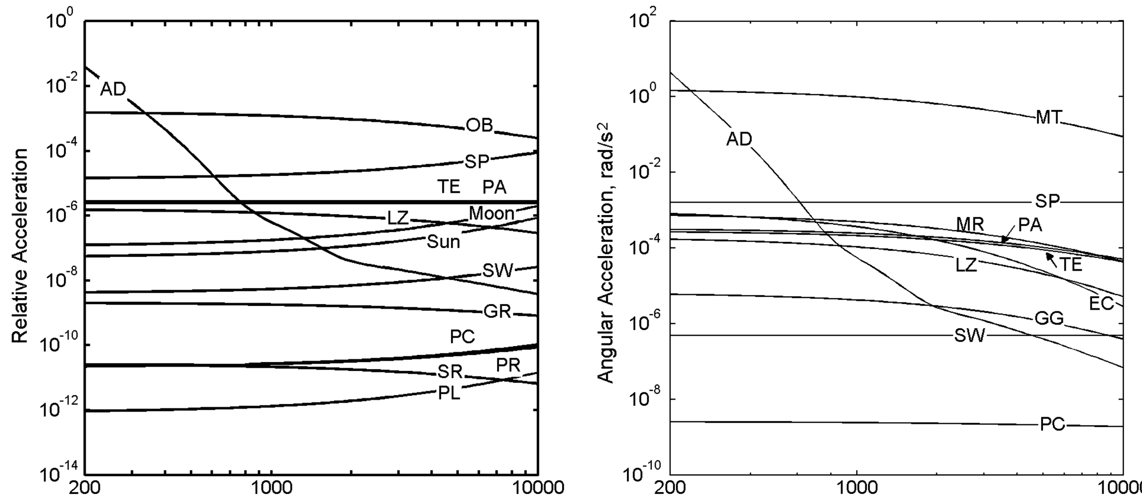


a) b)

**Fig. 14 Accelerations acting on a candidate spacecraft-on-chip architecture given as a function of altitude: a) orbital accelerations normalized to Earth's two-body gravity and b) angular accelerations.**

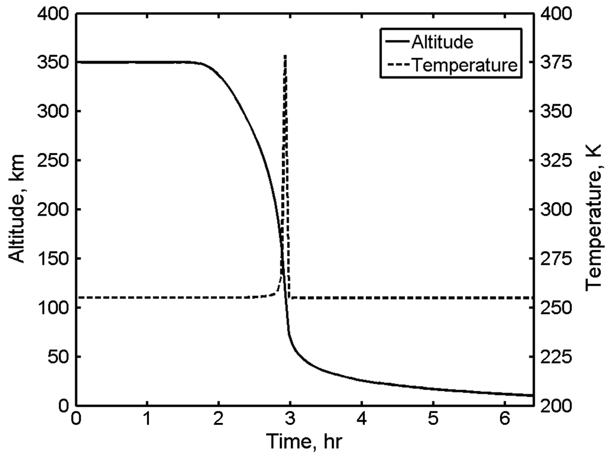


**Fig. 15 Time history of altitude and temperature for a simulated reentry maneuver of a candidate spacecraft-on-chip spacecraft.**

### C. Lorentz Force Spacecraft

The Lorentz force is responsible for capturing and ejecting electrostatically charged dust particles in the rings of Jupiter [65–67] and Saturn [68,69]. The dust particles attain time-varying charges that produce non-Keplerian orbits with altered orbital energy. If charge can be artificially generated on a spacecraft, it could serve as a means of propulsion. Previous research has explored the novel spacecraft maneuvers such a technology could enable [44,70–72]. Though a few architectures have been proposed to accommodate the self-capacitance and potential required for meaningful maneuvers, they require relatively large structures, such as groups of kilometer-long filaments. Based on this analysis and previous research [11], the $\lambda^{-3}$ scaling of $q/m$ implies that Lorentz force may instead be most easily achieved using a very small spacecraft.

Power represents a design challenge for equipping a spacecraft to propel itself via the Lorentz force. The spacecraft must produce enough power to maintain a net charge in spite of the near-Earth plasma environment that tends to discharge charge imbalances. The plasma environment discharges the spacecraft through so-called thermal and ram currents. These currents are functions of plasma characteristics, as well as the area of the charged spacecraft. That is, power requirements reduce according to an area-to-mass scaling. At small enough characteristic lengths, the discharge currents are characterized by the orbital-motion-limited regime, which reduces the power requirements even further.

A promising architecture proposed by Hoyt and Minor [73] requires only a power source and two plasma contactors to achieve a net charge. The following thought experiment, illustrated in Fig. 16, explains the concept. In a vacuum, if two conductive wires are connected to the terminals of a potential source (e.g. a battery or a solar cell), each wire can be thought of as reaching a potential equal to half of the source's potential and with opposing polarities. However, in a plasma environment, the wires' opposite polarities generate dissimilar plasma currents, resulting in dissimilar wire potentials

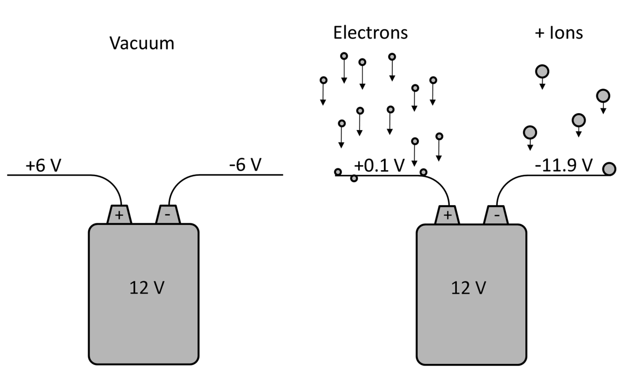


**Fig. 16 Equilibrium potentials for power supply terminals in a vacuum and plasma environment.**

[74]. Near-Earth, the positive wire would tend to discharge almost entirely. As long as the power source can supply sufficient current, the source would maintain the potential difference and would drive the potential to the negative wire. Such a spacecraft would carry a net negative charge that may be controlled through the power source.

Using this architecture, the candidate spacecraft-on-chip bus could be equipped for Lorentz propulsion using only two thin, conductive wires and a small solar-cell array. The wires act as plasma contactors and capacitors, and the solar cells produce the potential difference and current required to overcome plasma discharge currents. A previous study suggests that the candidate spacecraft-on-chip bus attached with two 1 m long wires and solar cells can achieve a $q/m$ on the order of a micro-Coulomb per kilogram. For a 500 km orbit, this $q/m$ is sufficient to produce daily growth of roughly 400 m of semimajor axis or 25 m of along-track motion.

## IX. Conclusions

The magnitude of orbital and angular accelerations in the near-Earth space environment can be highly dependent on the characteristic length $\lambda$ of the affected body. Most near-Earth perturbations can be modeled as pressures, in which case the critical ratio is the area-to-mass, which is dependent on $\lambda^{-1}$. The Lorentz force is dependent on the charge-to-mass ratio, which scales with $\lambda^{-2}$ in a vacuum. As $\lambda$ is reduced, these orbital and attitude accelerations become increasingly large, while gravitational accelerations remain unaffected. This understanding suggests which environmental forces and torques can and cannot be neglected for a given simulation and error tolerance. The analysis also identifies regions of characteristic length and altitude, within which different accelerations dominate the dynamics of a spacecraft.

A second design parameter is choice of geometry. This research offers a framework for considering a spacecraft geometry using a set nondimensional scale factors. With these scale factors, the results offered herein can be applied to an arbitrary geometry. Of the geometries considered here, a sphere and cube have fixed scale factors, while the scale factors for a square flat plate depend on thickness.

If $\lambda$ is sufficiently small for a selected geometry, nongravitational accelerations may reach magnitudes sufficient to enable new mission opportunities. By designing a spacecraft to have a very small $\lambda$, mission designers can potentially achieve novel spacecraft maneuvers passively and without the requirement of on-board fuel. A candidate spacecraft-on-chip bus is considered as a solar sail, a reentry vehicle, and a Lorentz propelled spacecraft. In each case, the magnitude of nongravitational acceleration suggests the potential for meaningful propellantless maneuvers.


## Acknowledgments

The authors wish to thank Zac Manchester, Sharon Kotz, Robert MacCurdy, and Alfred Ernst of Cornell University for their many contributions to this work. The authors also wish to thank Sandia National Laboratory's Center for Integrated Nanotechnology for their invaluable collaboration, expertise, and support.


## References


[1] Harwit, M., "Origins of the Zodiacal Dust Cloud," *Journal of Geophysical Research*, Vol. 68, No. 8, 1963, pp. 2171–2180. doi:10.1029/JZ068i008p02171

[2] Burns, J., Lamy, P., and Soter, S., "Radiation Forces on Small Particles in the Solar System," *Icarus*, Vol. 40, No. 1, 1979, pp. 1–48. doi:10.1016/0019-1035(79)90050-2

[3] Kresak, L., "Orbital Evolution of the Dust Streams Released from Comets," *Astronomical Institutes of Czechoslovakia Bulletin*, Vol. 27, No. 1, 1976, pp. 35–46.

[4] Colwell, J. E., Horanyi, M., and Grun, E., "Capture of Interplanetary and Interstellar Dust by the Jovian Magnetosphere," *Science*, Vol. 280, April 1998, pp. 88–91. doi:10.1126/science.280.5360.88

[5] Hamilton, D. P., and Burns, J. A., "Ejection of Dust from Jupiter's Gossamer Ring," *Nature*, Vol. 364, Aug. 1993, pp. 695–699.

doi:10.1038/364695a0
[6] Whipple, F. L., "Theory of Micro-Meteorites, 1: In an Isothermal Atmosphere," *Proceedings of the National Academy of Sciences*, Vol. 36, No. 12, 1950, pp. 687–695.
[7] Beech, M., "Finite-Size Corrections to the Atmospheric Heating of Micrometeorites," *Monthly Notices of the Royal Astronomical Society*, Vol. 402, No. 2, 2010, pp. 1208–1212. doi:10.1111/j.1365-2966.2009.15968.x
[8] Barnhart, D., Vladimirova, T., and Sweeting, M., "Very-Small-Satellite Design for Distributed Space Missions," *Journal of Spacecraft and Rockets*, Vol. 44, No. 6, 2007, pp. 1294–1306. doi:10.2514/1.28678
[9] Barnhart, D., Vladimirova, T., and Sweeting, M., "Satellite Miniaturization Techniques for Space Sensor Networks," *Journal of Spacecraft and Rockets*, Vol. 46, No. 2, 2009, pp. 469–472. doi:10.2514/1.41639
[10] Atchison, J. A., and Peck, M. A., "A Passive, Sun-Pointing, Millimeter-Scale Solar Sail," *Acta Astronautica*, Vol. 67, Nos. 1-2, 2010, pp. 108–121. doi:10.1016/j.actaastro.2009.12.008
[11] Atchison, J. A., and Peck, M. A., "A Millimeter-Scale Lorentz-Propelled Spacecraft," AIAA Paper 2007-6847, 2007.
[12] Janson, S. W., "Mass-Producible Silicon Spacecraft for 21st Century Missions," AIAA Paper 99-4458, AIAA Space Technology Conference and Exposition, Albuquerque, NM, 1999.
[13] Janson, S. W., Helvajian, H., and Breuer, K., "MEMS, Micro-engineering and Aerospace Systems," AIAA Paper A99-33749, 30th AIAA Fluid Dynamics Conference, Norfolk, VA, 1999, pp. 1–12.
[14] Janson, S. W., "Micro/Nanotechnology for Micro/Nano/Picosatellites," AIAA Paper 2003-6269, Space 2003, Long Beach, CA, 2003, pp. 1–11.
[15] Miller, L. M., "MEMS for Space Applications," *Proceedings of Society of Photographic Instrumentation Engineers (SPIE)*, Vol. 3680, Paris, April 1999, pp. 1–13.
[16] Longuski, J. M., Todd, R. E., and König, W. W., "Survey of Nongravitational Forces and Space Environmental Torques: Applied to the Galileo," *Journal of Guidance, Control, and Dynamics*, Vol. 15, No. 3, 1992, pp. 545–553. doi:10.2514/3.20874
[17] Heidt, H., Puig-Suari, J., Moore, A. S., Nakasuka, S., and Twiggs, R. J., "Cubesat: A New Generation of Picosatellite for Education and Industry Low-Cost Space Experimentation," AIAA Paper SSC00-V-5, AIAA/Utah State Univ. Conference on Small Satellites, Aug. 2001.
[18] Hughes, P. C., "Attitude Motion Equations," *Spacecraft Attitude Dynamics*, Dover, New York, 2004, pp. 39–83, Chap. 3.
[19] Vallado, D. A., "Three-Body and $n$-Body Equations," *Fundamentals of Astrodynamics and Applications*, 2nd ed., Microcosm, El Segundo, CA, 2004, pp. 33–48, Chap. 1.4.
[20] Hughes, P. C., "Spacecraft Torques," *Spacecraft Attitude Dynamics*, Dover, New York, 2004, pp. 233–280, Chap. 8.
[21] McCarthy, D. D., and Petit, G. (eds.), "General Relativistic Models for Space-Time Coordinates and Equations of Motion," *International Earth Rotation and Reference Systems Service*, TN 32, 2003, pp. 104–108.
[22] Mashoon, B., Helh, F. W., and Theiss, D. S., "The Lense–Thirring Papers," *General Relativity and Gravitation*, Vol. 16, No. 8, 1984, pp. 711–750. doi:10.1007/BF00762913; also Lense, J., and Thirring, H., "On the Influence of the Proper Rotation of Central Bodies on the Motions of Planets and Moons According to Einstein's Theory of Gravitation," *Zeitschrift fur Physik D: Atoms, Molecules and Clusters*, Vol. 19, 1918, pp. 156–163.
[23] Vallado, D. A., "Disturbing Forces," *Fundamentals of Astrodynamics and Applications*, 2nd ed., Microcosm, El Segundo, CA, 2004, pp. 550–551, Chap. 8.6.
[24] Storch, J. A., "Aerodynamic Disturbances on Spacecraft in Free-Molecular Flow," Aerospace Corp., Rept. No TR-2003(3397)-1, Oct. 2002, pp. 1–70.
[25] King-Hele, D. G., "Evaluation of Drag Coefficient," *Satellite Orbits in an Atmosphere: Theory and Application*, Blackie and Sons, Glasgow, 1987, Chap. 2.3.
[26] Cook, G. E., "Satellite Drag Coefficients," *Planetary Space Science*, Vol. 13, No. 10, 1965, pp. 929–946. doi:10.1016/0032-0633(65)90150-9
[27] Cour-Palais, B. G., "Meteoroid Environment Model: 1969 (Near Earth to Lunar Surface)," NASA SP-8013, March 1969.
[28] Wertz, J. R., "Solar Radiation and the Solar Wind," *Spacecraft Attitude Determination and Control*, edited by D. Reidel, Dordrecht, Holland, The Netherlands, 1978, pp. 129–132, Chap. 5.3.
[29] McInnes, C. R., *Solar Sailing: Technology, Dynamics and Mission Applications*, Springer–Verlag, New York, 1999, pp. 1–296.
[30] Blanco, V. M., and McCuskey, S. W., *Basic Physics of the Solar System*, Addison Wesley Longman, Reading, MA, 1961, pp. 50–52.
[31] Antreasian, P. G., and Rosborough, G. W., "Prediction of Radiant Energy Forces on the TOPEX/POSEIDON Spacecraft," *Journal of Spacecraft and Rockets*, Vol. 29, No. 1, 1992, pp. 81–90. doi:10.2514/3.26317
[32] Robertson, H. P., "Dynamical Effects of Radiation in the Solar System," *Monthly Notices of the Royal Astronomical Society*, Vol. 97, No. 6, 1937, pp. 423–438.
[33] Bottke, W. F., Vokrouhlicky, D., Rubincam, D. P., and Nesvorny, D., "The Yarkovsky and YORP Effects: Implications for Asteroid Dynamics," *Annual Review of Earth and Planetary Sciences*, Vol. 34, No. 1, 2006, pp. 157–191. doi:10.1146/annurev.earth.34.031405.125154
[34] Peterson, C., "A Source Mechanism for Meteorites Controlled by the Yarkovsky Effect," *Icarus*, Vol. 29, No. 1, 1976, pp. 91–111. doi:10.1016/0019-1035(76)90105-6
[35] Griffins, D. J., "The Field of a Magnetized Object," *Introduction to Electrodynamics*, 3rd ed., Prentice–Hall, Upper Saddle River, NJ, 1999, pp. 263–268, Chap. 6.2.
[36] Yung, K. W., Landecker, P. B., and Villani, D. D., "An Analytic Solution for the Force Between Two Magnetic Dipoles," *Magnetic and Electrical Separation*, Vol. 9, No. 1, 1998, pp. 39–52. doi:10.1155/1998/79537
[37] Parker, R. J., "Permanent Magnets and the Laws of Electromagnetic Scaling," *Advances in Permanent Magnetism*, Wiley, New York, 1990, pp. 179–181, Chap. 6.7.
[38] Griffins, D. J., "Electrodynamics," *Introduction to Electrodynamics*, 3rd ed., Prentice–Hall, Upper Saddle River, NJ, 1999, pp. 263–268, chap. 7.
[39] Parker, R. J., "Magnetic and Physical Property Tables," *Advances in Permanent Magnetism*, Wiley, New York, 1990, pp. 316–322, Appendix 2.
[40] Schalkowsky, S., and Harris, M., "Spacecraft Magnetic Torques," *NASA Space Vehicle Design Criteria*, NASA SP-8018, March 1969, pp. 1–51.
[41] Eterno, J. S., "Attitude Determination and Control," *Space Mission Analysis and Design*, 3rd ed., Microcosm, El Segundo, CA, 2005, pp. 354–381, chap. 11.1.
[42] Wilson, R. H., "Rotational Magnetodynamics and Steering of Space Vehicles," NASA TN D-566, Sept. 1961, pp. 1–23.
[43] Sehnal, L., "The Motion of a Charged Satellite in the Earth's Magnetic Field," *Smithsonian Astrophysical Observatory Special Report No. 271*, April 1969, pp. 1–15.
[44] Streetman, B., and Peck, M., "New Synchronous Orbits Using the Geomagnetic Lorentz Force," *Journal of Guidance, Control, and Dynamics*, Vol. 30, No. 6, 2007, pp. 1677–1690. doi:10.2514/1.29080
[45] Hwang, C., and Mascagni, M., "Electrical Capacitance of the Unit Cube," *Journal of Applied Physics*, Vol. 95, No. 7, April 2004, pp. 3798–3902. doi:10.1063/1.1664031
[46] Read, F. H., "Capacitances and Singularities of the Unit Triangle, Square, Tetrahedron and Cube," *Journal of Electrostatics*, Vol. 62, No. 1, Sept. 2004, pp. 51–62. doi:10.1016/j.elstat.2004.04.005
[47] Tikhonov, A. A., "A Method of Semipassive Attitude Stabilization of a Spacecraft in the Geomagnetic Field," *Cosmic Research (Translation of Kosmicheskie Issledovaniya)*, Vol. 41, No. 1, 2003, pp. 63–73. doi:10.1023/A:1022355730291
[48] Lemoine, F. G., Kenyon, S. C., Factor, J. K., Trimmer, R. G., Pavlis, N. K., Chinn, D. S., Cox, C. M., Klosko, S. M., Luthcke, S. B., Torrence, M. H., Wang, Y. M., Williamson, R. G., Pavlis, E. C., Rapp, R. H., and T. R. Olson, "The Development of the Joint NASA GSFC and NIMA Geopotential Model EGM96," NASA TP-1998-206861, Greenbelt, MD, July 1998.
[49] Barton, C. E., "International Geomagnetic Reference Field: The Seventh Generation," *Journal of Geomagnetism and Geoelectricity*, Vol. 49, No. 2, 1997, pp. 123–148.
[50] "U.S. Standard Atmosphere 1976," NASA TM-X-74335, Oct. 1976.
[51] Allen, C. W., "Extensions of Earth Atmosphere and Distribution with Height," *Astrophysical Quantities*, Univ. of London, Athlone, Ireland, U.K., 1976, chap. 6.
[52] Cole, G. H. A., and Woolfson, M. M., "Planetary Albedoes," *Planetary Science: The Science of Planets Around Stars*, Institute of Physics Publishing, London, 2002, pp. 380–382.

[53] Gilmore, D. G., Hardt, B. E., Prager, R. C., Grob, E. W., and Ousley, W., "Thermal," *Space Mission Analysis and Design*, 3rd ed., Microcosm, El Segundo, CA, 2005, p 433, Chap. 11.5.
[54] Reeves, E. I., "Spacecraft Design and Sizing," *Space Mission Analysis and Design*, Kluwer Academic, Norwell, MA, 1999, pp. 301–352.
[55] Bauccio, M., "Electrical Resistivity of Metals," *ASM Metals Reference Book*, 3rd ed., ASM International, Materials Park, OH, 1993, pp. 157–158.
[56] Greschik, G., "Solar Sail Scalability and a 'Truly Scalable' Architecture: The Space Tow," *Journal of Spacecraft and Rockets*, Vol. 44, No. 4, 2007, pp. 831–839.
doi:10.2514/1.26556
[57] Jack, C., and Welch, C. S., "Solar Kites: Small Solar Sails with no Moving Parts," *Acta Astronautica*, Vol. 40, Nos. 2-8, 1997, pp. 137–142.
doi:10.1016/S0094-5765(97)00120-3
[58] Lappas, V., Wie, B., McInnes, C. R., Tarabini, L., Gomes, L., and Wallace, K., "Microsolar Sails for Earth Magnetotail Monitoring," *Journal of Spacecraft and Rockets*, Vol. 44, No. 4, 2007, pp. 840–848.
doi:10.2514/1.23456
[59] Prucey, R., Morcone, J., and Murphy, D., "NASA Nanosatellites Catch Ride on Rocket, Demonstrate Technology," NASA Press Release H-08-70AR, 31 July 2008.
[60] Wehry, A., and Mann, I., "Identification of $\beta$-Meteoroids from Measurements of the Dust Detector Onboard the Ulysses Spacecraft," *Astronomy and Astrophysics*, Vol. 341, No. 1, 1999, pp. 296–303.
[61] Berg, O. E., and Grun, E., "Evidence of Hyperbolic Cosmic Dust Particles," *Space Research 13*, edited by M. J. Rycroft and S. K. Runcorn, Akademie Verlag, Berlin, 1973, pp. 1047–1055.
[62] Koppenwallner, G., Fritsche, B., and Lips, T., "Survivability and Ground Risk Potential of Screws and Bolts of Disintegrating Spacecraft During Uncontrolled Re-Entry," *Proceedings of the Third European Conference on Space Debris*, ESA SP-473, 2001, pp. 533–539.
[63] Griffin, M. D., and French, J. R., "Atmospheric Entry," *Space Vehicle Design*, 2nd ed., AIAA, Reston, VA, 2004, chap. 11, pp. 305–320.
[64] Love, S. G., and Brownlee, D. E., "A Direct Measurement of the Terrestrial Mass Accretion Rate of Cosmic Dust," *Science*, Vol. 262, No. 5133, Oct. 1993, pp. 550–553.
doi:10.1126/science.262.5133.550
[65] Grun, E., Kruger, H., Graps, A. L., Hamilton, D. P., Heck, A., Linkert, G., Zook, H. A., Dermott, S., Fechtig, H., Gustafson, B. A., Hanner, M. S., Horányi, M., Kissel, J., Lindblad, B. A., Linkert, D., Mann, I., McDonnell, J. A. M., Morfill, G. E., Polanskey, C., Schwehm, G., and Srama, R., "Galileo Observes Electromagnetically Coupled Dust in the Jovian Magnetosphere," *Journal of Geophysical Research*, Vol. 103, No. E9, 1998, pp. 20011–20022.
doi:10.1029/98JE00228
[66] Colwell, J. E., Horanyi, M., and Grun, E., "Capture of Interplanetary and Interstellar Dust by the Jovian Magnetosphere," *Science*, Vol. 280, April 1998, pp. 88–91.
doi:10.1126/science.280.5360.88
[67] Schaffer, L., and Burns, J. A., "The Dynamics of Weakly Charged Dust: Motion Through Jupiter's Gravitational and Magnetic Fields," *Journal of Geophysical Research*, Vol. 92, No. A3, 1987, pp. 2264–2280.
doi:10.1029/JA092iA03p02264
[68] Horanyi, M., "Charged Dust Dynamics in the Solar System," *Astronomy and Astrophysics* Annual Reviews, Vol. 34, No. 1, 1996, pp. 383–418.
doi:10.1146/annurev.astro.34.1.383
[69] Bradford A. S., Soderblom, L., Beebe, R., Boyce, J., Briggs, G., Bunker, A., Collins, S. A., Hansen, C. J., Johnson, T. V., Mitchell, J. L., Terrile, R. J., Carr, M., Cook, A. F., II, Cuzzi, J., Pollack, J. B., Danielson, G. E., Ingersoll, A., Davies, M. E., Hunt, G. E., Masursky, H., Shoemaker, E., Morrison, D., Owen, T., Sagan, C., Veverka, J., Strom, R., and Suom, V. E., "Encounter with Saturn: Voyager 1 Imaging Science Results," *Science*, Vol. 212, No. 4491, 1981, pp. 163–191.
doi:10.1126/science.212.4491.163
[70] Streetman, B., and Peck, M., "A General Bang-Bang Control Method for Lorentz Augmented Orbits," American Astronomical Society Paper 08-111, American Astronautical Society Spaceflight Mechanics Meeting, Galveston, TX, 27–31 Jan. 2008.
[71] Atchison, J. A., and Peck, M., "Lorentz Augmented Jovian Orbit Insertion," *Journal of Guidance, Control, and Dynamics*, Vol. 32, No. 2, March 2009, pp. 418–423.
doi:10.2514/1.38406
[72] Streetman, B., and Peck, M., "Gravity-Assist Maneuvers Augmented by the Lorentz Force," *Journal of Guidance, Control, and Dynamics*, Vol. 32, No. 5, 2009, pp. 1639–1647.
doi:10.2514/1.35676
[73] Hoyt, R. P., and Minor, B. M., "Remediation of Radiation Belts Using Electrostatic Tether Structures," *Proceedings of Institute of Electrical and Electronics Engineers Aerospace Conference*, 2005, pp. pp. 583–594.
[74] Hillard, G. B., and Ferguson, D. C., "Low Earth Orbit Spacecraft Charging Design Guidelines," NASA TP-2003-212287, Feb. 2003.